Islanding Detection With Positive Feedback of Selected Frequency for DC Microgrid Systems

Qinghui Huang, *Student Member, IEEE*, Hongyi Chen, *Student Member, IEEE*, Xin Xiang, *Member, IEEE*, Chushan Li, *Member, IEEE*, Wuhua Li, *Member, IEEE*, and Xiangning He, *Fellow, IEEE*

***Abstract*—The oscillation frequency of the point of common coupling (PCC) voltage is proposed as a new detecting freedom for dc-based islanding events in this article. In the presented method, the voltage positive feedback with a frequency selection is applied to a distributed generator to make the PCC voltage oscillate at the selected frequency when islanding events occur. With the frequency information, islanding events can be identified by the small-amplitude oscillation superimposed on the normal dc voltage without the necessity of voltage amplitude to be shifted out of the normal range. Thus, the islanding events can be effectively distinguished from other abnormal conditions that lead to large voltage fluctuations, and so, the accuracy of islanding detection is improved. Also, the power quality at islanding events is enhanced, which provides important benefits for seamless transfer from the unintentional islanding conditions to the controlled islanding conditions. Moreover, the frequency selection is designed to only transfer the voltage signal at the sensitive frequency band of the islanding condition. As a result, the deterioration of stability caused by the voltage positive feedback can be relieved under the grid-connected condition compared to the existing methods. Finally, the effectiveness of the proposed method has been verified by both time-domain nonlinear simulation and experimental results.**

***Index Terms*—DC microgrid, islanding detection, positive feedback, selected frequency.**

NOMENCLATURE

$P_{\rm ref}$	Reference of command to power control loop.
P	DG injected power (W).
$P_{\rm dis}$	Disturbance to reference of power command.
$I_{\rm ref}$	Reference of command to current control loop.
I	DG injected current (A).
$I_{\rm dis}$	Disturbance to reference of current command.
V	Voltage at the point of common coupling (V).
L	DG filter inductance (H).
C	Filter capacitance and dc-bus capacitance (F).
R_L	Load resistance (Ω).
V_g	DC grid voltage (V).
I_g	DC grid current (A).
$\sim$	Small-signal disturbance.
R_g	Resistance of dc grid transmission line (Ω).
L_g	Inductance of dc grid transmission line (H).
s	Laplace operator.
K_{pp}	Power control loop proportional constant.
K_{pi}	Power control loop integral constant.
K_{cp}	Current control loop proportional constant.
K_{ci}	Current control loop integral constant.
f_0	Set value of selected resonant frequency (Hz).
K_r	Gain constant of resonator.
ω_i	Control bandwidth of resonator.
ω_o	Resonant angular frequency of resonator (rad/s).

Manuscript received November 4, 2020; revised January 25, 2021; accepted March 3, 2021. Date of publication March 17, 2021; date of current version June 30, 2021. This work was supported in part by the National Nature Science Foundation of China under Grants 51925702 and U1834205 and in part by the Zhejiang Provincial Key Research and Development Program under Grant 2018C01SA150059. This article was presented in part at the IEEE Applied Power Electronics Conference and Exposition, New Orleans, LA, USA, Mar. 15–20, 2020, entitled "*Islanding Detection Methods Based on Self-Oscillation of Particular Frequency in DC Distribution Systems*." Recommended by Associate Editor Y. Yang. *(Corresponding authors: Wuhua Li; Xin Xiang.)*

Qinghui Huang, Hongyi Chen, Xin Xiang, Wuhua Li, and Xiangning He are with the College of Electrical Engineering, Zhejiang University, Hangzhou 310027, China (e-mail: qinghuihuang@zju.edu.cn; hongyi.chen@zju.edu.cn; xiangxin@zju.edu.cn; woohualee@zju.edu.cn; hxn@zju.edu.cn).

Chushan Li is with the Zhejiang University–University of Illinois at Urbana-Champaign Institute, Zhejiang University, Haining 314400, China (e-mail: chushan@intl.zju.edu.cn).

Color versions of one or more figures in this article are available at https://doi.org/10.1109/TPEL.2021.3066486.

Digital Object Identifier 10.1109/TPEL.2021.3066486

I. INTRODUCTION

MICROGRIDS are widely regarded as an effective way that caters to the high penetration of distributed renewable resources [1], [2], enhances energy efficiency [3], and improves power-supply quality as well as reliability [4], [5].

AC microgrids that can integrate the renewable energy generation and conventional electrical equipment have been extensively studied in the past decade and some of them are practically applied [6]–[9]. However, with the increasing proportion of intrinsically dc sources and loads in the power system, such as photovoltaics, fuel-cells, electric vehicles, electronic-products, etc., dc microgrids have shown more advantages of higher efficiency and lower cost than ac counterparts because of the absence of ac/dc and dc/ac conversion stages [10]. Besides, there are no synchronization and reactive power compensation problems in the dc-based system [11], which effectively reduces the system complexity. These benefits make dc microgrids attract great attention in recent years as a promising component in modern power systems [12]–[14].

The protection issues are the key factors that restrict the large-scale application of dc systems [15], [16]. Islanding detection is an important functional requirement to ensure the safety of customer equipment and humans during unintentional islanding conditions [17]–[19]. In this case, there are only distributed generators (DGs) energizing the load, and the point of common

coupling (PCC) voltage is out of control due to the loss of the utility. Active islanding detection methods (IDMs) are necessary to diminish the nondetection zone of passive IDMs when the power generation is close to the consumption at an islanding event [20], [21]. Although originally defined in ac systems, the islanding event is also essential to be detected in dc microgrids. Unfortunately, it is much more difficult to be detected in dc systems than that in ac counterparts, because the synchronized information is insufficient for dc systems.

An impedance-based islanding detection scheme is proposed [22] in which a DG actively injects a sinusoidal current disturbance to obtain the equivalent impedance seen from the DG converter by calculating *dv/di*. This method could detect the islanding condition quickly as the ac impedance of the dc grid is almost equivalent to short circuit under the grid-connected condition but open circuit when the islanding event occurs. However, the detecting threshold with open-loop disturbance is hard to set due to the variation of the system impedance [20].

The methods with positive feedback are widely applied in the ac system to improve the detecting accuracy and simplify the parameter design, especially the detecting thresholds [23]. The disturbance is positively correlated with the monitoring variables, which indicate islanding events at the last moment in these schemes. The voltage positive feedback for islanding detection is first applied in dc systems by imposing a square wave perturbation on the current command of a DG, and the amplitude of perturbation is added as a constant once the fluctuation of the PCC voltage increases during the last period [24]. In the case of islanding, the amplitude of the PCC voltage shall be shifted out of the normal range as an islanding signal because of the lack of voltage regulation. Unfortunately, the appropriate frequency design of the disturbance and system stability is not fully analyzed due to the nonlinearity between the disturbance and the PCC voltage. An IDM with the voltage positive feedback of full frequency-band (VPFOFF) is proposed [25] in which a perturbation proportional to the deviation of voltage at the PCC from the normal value is injected to the reference command of power or current control loop to constitute voltage positive feedback. The PCC voltage begins to oscillate at the islanding events until its amplitude is out of the normal range. It has benefits of the detailed feedback gain design and stability analysis by modeling the system, but the oscillating frequency of voltage at islanding events is unknown and could not be utilized for islanding detection.

In this article, an IDM with the voltage positive feedback of selected frequency (VPFOSF) is proposed. A sinusoidal self-excited oscillator is designed and a frequency selection is inserted into the voltage positive feedback loop to ensure the selected frequency oscillation in the case of islanding. On the one hand, this frequency information can be perceived in the divergent oscillation even when the amplitude of the fluctuation is small, and this is advantageous over the existing methods which usually require shifting voltage amplitude out of the normal range for islanding detection. Because of this benefit, islanding events can be readily distinguished from other abnormal conditions which may lead to large voltage fluctuation. Therefore, the detection accuracy is enhanced and power quality during the seamless transfer would be improved because of the much less voltage fluctuation than the existing methods. On the other hand, since the frequency bands of the PCC voltage sensitive to the disturbances under the islanding condition and grid-connected condition are clearly different, the frequency selection is designed to only transfer the disturbance at the most sensitive frequency of the islanding condition and attenuate that of the grid-connected condition. In this manner, the stability deterioration under the grid-connected condition would be more relieved compared to the VPFOFF scheme.

The sensitivity of the PCC voltage to the disturbances in the frequency domain under the islanding condition and grid-connected condition is analyzed in detail in Section II. The concept and implementation of islanding detection with the VPFOSF are also explained in this section. The parameters design of frequency selection in the single-DG system is given in Section III, and their influence on the stability of the grid-connected condition and the islanding detecting speed is also provided. The application of the proposed method for the multiple-DG system is extended in Section IV. The simulation and experimental results are given in Sections V and VI, respectively, to validate the effectiveness and robustness of the proposed approach under various operating conditions. Finally, VII concludes the article.

II. Proposed IDM

The key principle of most active IDMs is to inject perturbation to cause the fluctuation of the PCC voltage, and the system state is then judged by the difference of voltage between the islanding condition and grid-connected condition. Thus, it is necessary to analyze the sensitivity of the PCC voltage to the disturbance components in the frequency domain since it facilitates the choice and design of the disturbance frequency and also reveals the frequency-band where the DG with the voltage positive feedback is most likely to oscillate at the islanding events.

A. System Description

Although there exist various converters with different topologies and control strategies in dc systems, they can be classified into two types according to the control targets—one responsible for the regulation of the PCC voltage and another taking charge of delivering constant power [27]. A dc system, the same as mentioned in the VPFOFF scheme, is adopted in this article for contrast. The system consists of one power source and one voltage source, both of which energize the load together, as exhibited in Fig. 1 [25]. A DG is modeled as the power source P_{DG} to deliver the constant power to the load. The load is represented by the resistance R_L to investigate the condition that has the largest nondetection zone [19]. The utility and interface converter is modeled as a dc grid V_g with the transmission line Z_g to regulate the PCC voltage under the grid-connected condition [28]. R_g represents the resistance of the dc grid transmission line and L_g is the inductance of the dc grid transmission line. The capacitance C denotes the filter capacitance of the DG and the bus capacitance.

The control strategy of the DG made up of the current inner loop and power outer loop is displayed in Fig. 2. Two PI

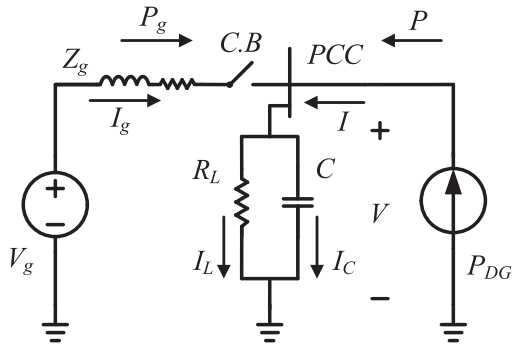

Fig. 1. Equivalent model of dc microgrid for islanding detection.

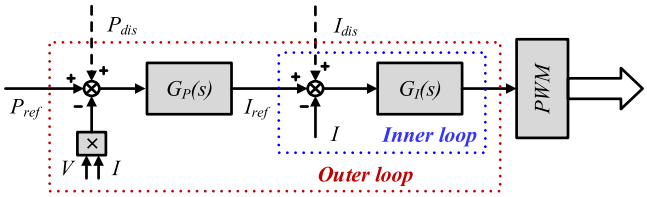

Fig. 2. Control strategy diagram of DG with current inner loop and power outer loop.

compensators ($G_P(s) = K_{pp}+K_{pi}/s$, $G_I(s) = K_{cp}+K_{ci}/s$) are adopted to regulate the injected power and current of the DG. K_{pp} and K_{pi} are power control loop proportional constant and integral constant, respectively. K_{cp} and K_{ci} are current control loop proportional constant and integral constant, respectively.

When the power of generation and consumption exactly match is the hardest case for islanding detection due to no voltage variation at an islanding event. Then, this model linearized at the power matching condition (P_0, I_0, R_0) is given by [25]

$$\widetilde{I}_{ref} = G_P(s)\left(\widetilde{P}_{ref} - \widetilde{P}\right) \tag{1}$$

$$\widetilde{I} = \widetilde{I}_{ref} \tag{2}$$

$$\widetilde{P} = I_0\,\widetilde{V} + V_0\,\widetilde{I} \tag{3}$$

$$\widetilde{I} = \frac{\widetilde{V}}{R_L} + \widetilde{V}\,sC + \frac{\widetilde{V}}{R_g + sL_g}. \tag{4}$$

Although the small-signal model is only valid at its equilibrium [26], the proposed IDM can be effective under most conditions since the hardest case for islanding detection is taken into consideration. The current loop is simplified due to its much faster dynamics compared to that of the power loop. When the islanding event occurs, only the DG is energizing the load. Then, (4) during the islanding mode can be modified as

$$\widetilde{I} = \frac{\widetilde{V}}{R_L} + \widetilde{V}\,sC. \tag{5}$$

There are two kinds of disturbing components, current disturbance I_{dis} or power disturbance P_{dis}, which can be used to disturb the reference of the inner loop or outer loop for islanding detection, respectively, as shown in Fig. 2. When the current loop is disturbed, (2) can be rewritten as

$$\widetilde{I} = \widetilde{I}_{ref} + \widetilde{I}_{dis}. \tag{6}$$

When the power disturbing scheme is adopted, (1) can be rewritten as

$$\widetilde{I}_{ref} = G_P(s)\left(\widetilde{P}_{ref} + \widetilde{P}_{dis} - \widetilde{P}\right). \tag{7}$$

B. Sensitivity of PCC Voltage to Disturbance Components

The variation of the reference of power loop $\tilde{P}_{\rm ref}$ is set to zero while investigating the impact of the disturbance components. Solving (1), (3), (5), (6) and (1), (3), (4), (6), respectively, the transfer functions from the current disturbance to the PCC voltage under the islanding and grid-connected conditions can be derived as follows:

$$\begin{aligned} G_{In\_island} &= \frac{\widetilde{V}}{\widetilde{I}_{dis}} = \frac{a_1 s}{b_2 s^2 + b_1 s + b_0} \\ a_1 &= R_L, b_2 = CR_L + CK_{pp}R_L V_0 \\ b_1 &= 1 + I_0 K_{pp} R_L + K_{pp} V_0 + CK_{pi} R_L V_0 \\ b_0 &= I_0 K_{pi} R_L + K_{pi} V_0 \end{aligned} \tag{8}$$

$$\begin{aligned} G_{In\_grid} &= \frac{\widetilde{V}}{\widetilde{I}_{dis}} = \frac{a_2 s^2 + a_1 s}{b_3 s^3 + b_2 s^2 + b_1 s + b_0} \\ a_2 &= R_L L_g, a_1 = R_L R_g \\ b_3 &= CL_g R_L + CK_{pp} L_g R_L V_0 \\ b_2 &= L_g + I_0 K_{pp} L_g R_L + CR_g R_L \\ &\quad + K_{pp} L_g V_0 + CK_{pi} L_g R_L V_0 + CK_{pp} R_g R_L V_0 \\ b_1 &= R_g + R_L + I_0 K_{pi} L_g R_L + I_0 K_{pp} R_g R_L \\ &\quad + K_{pi} L_g V_0 + K_{pp} R_g V_0 + K_{pp} R_L V_0 \\ &\quad + CK_{pi} R_g R_L V_0 \\ b_0 &= I_0 K_{pi} R_g R_L. \end{aligned} \tag{9}$$

The derived and measured frequency responses from the current disturbance to the PCC voltage under the islanding condition and grid-connected condition are plotted in Fig. 3 using the No.1 parameters of the simulation in Table I. The measured data are based on the nonlinear model in Simulink by injecting small disturbances at different frequencies. The derived model agrees with the measured one, which proves the correctness of the derived model. These parameters are also used in the numerical studies of the single system in the rest of this article. The magnitude of voltage sensitivity under the islanding condition is much larger than that of the grid-connected condition at the low-frequency band (under 105 Hz). This indicates that the PCC voltage is much easier to be disturbed by the current disturbance at the low-frequency range in the case of islanding. The maximum magnitude of the islanding condition is at around 60 Hz where the phase is close to 0°. This means that this frequency is the easiest to be disturbed and is the most likely to oscillate at the islanding events when the DG is equipped with the VPFOFF. However, the most sensitive frequency of the

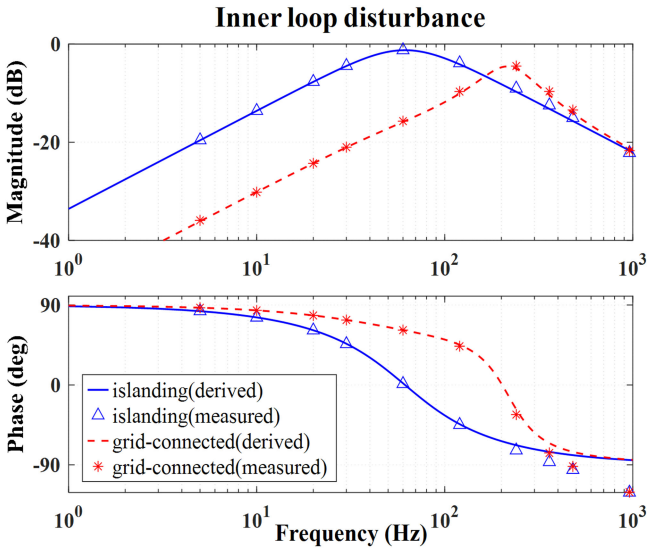

Fig. 3. Frequency response from current disturbance to PCC voltage.

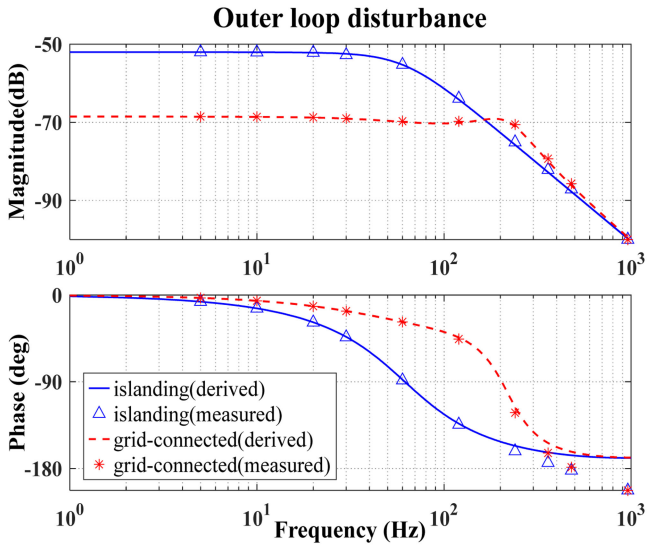

Fig. 4. Frequency response from power disturbance to PCC voltage.

TABLE I
SIMULATION AND EXPERIMENTAL PARAMETERS OF DC SYSTEM

Items	Simulation values		Experiment values
	No.1	No.2	
Dc grid rated voltage V_g (V)	500		200
Feeder impedance Z_g (Ω/mH)	0.22/0.3	0.22/0.3	0
Rated load resistance R_L (Ω)	2.5	2	50
DG rated voltage (V)	600	600	300
DG rated power P_0 (kW)	100	125	0.8
DG filter inductance L (mH)	2	4	2.4
DG switching frequency (kHz)	10	10	10
Dc-bus capacitance C (μF)	2000	4000	110
Power loop constant K_{pp}	1.2*10^{-5}	1.2*10^{-5}	0.005
Power loop constant K_{pi}	0.75	0.75	0.5
Current loop constant K_{cp}	0.0249	0.0249	0.0593
Current loop constant K_{ci}	18.77	18.77	44.78

grid-connected mode is approximately 110 Hz. When the positive voltage feedback IDM is adopted, this difference between the two conditions makes it possible to improve the stability of the grid-connected condition without an impact on the islanding detection, if the feedback path is designed to attenuate the signal at the most sensitive frequency of the grid-connected condition and transfer the signal at the most sensitive frequency of the islanding condition.

Solving (2), (3), (5), (7) and (2), (3), (4), (7), respectively, the transfer functions from power disturbance to the PCC voltage during the islanding mode and grid-connected mode can be given by

$$G_{Out\_island} = \frac{\tilde{V}}{\tilde{P}_{dis}} = \frac{a_1 s + a_0}{b_2 s^2 + b_1 s + b_0}$$
$$a_1 = R_L K_{pp}, a_0 = R_L K_{pi}$$
$$b_2 = CR_L + CK_{pp} R_L V_0$$
$$b_1 = 1 + I_0 K_{pp} R_L + K_{pp} V_0 + CK_{pi} R_L V_0$$
$$b_0 = I_0 K_{pi} R_L + K_{pi} V_0 \quad (10)$$

$$G_{Out\_grid} = \frac{\tilde{V}}{\tilde{P}_{dis}} = \frac{a_2 s^2 + a_1 s + a_0}{b_3 s^3 + b_2 s^2 + b_1 s + b_0}$$
$$a_2 = K_{pp} L_g R_L, a_1 = K_{pi} L_g R_L + K_{pp} R_g R_L$$
$$a_0 = K_{pi} R_g R_L$$
$$b_3 = CL_g R_L + CK_{pp} L_g R_L V_0$$
$$b_2 = L_g + I_0 K_{pp} L_g R_L + CR_g R_L + K_{pp} L_g V_0 + CK_{pi} L_g R_L V_0 + CK_{pp} R_g R_L V_0$$
$$b_1 = R_g + R_L + I_0 K_{pi} L_g R_L + I_0 K_{pp} R_g R_L + K_{pi} L_g V_0 + K_{pp} R_g V_0 + K_{pp} R_L V_0 + CK_{pi} R_g R_L V_0$$
$$b_0 = I_0 K_{pi} R_g R_L + K_{pi} R_g V_0 + K_{pi} R_L V_0. \quad (11)$$

The derived and measured frequency responses from the power disturbance to the PCC voltage in the islanding and grid-connected cases are demonstrated in Fig. 4. The two responses reach a good agreement, and hence, the correctness of the derived model is validated. The PCC voltage is much easier to be disturbed by the power disturbance at the low-frequency band. The most sensitive frequencies of the islanding mode and grid-connected mode are both at 0 Hz where the magnitude is the maximum and the phase is close to 0°.

C. Implementation of Proposed Islanding Detection

The proposed IDM is to realize that the selected frequency oscillation occurs to indicate the islanding events. Then, a frequency selection is inserted into the voltage feedback loop to achieve a sinusoidal self-excited oscillator, as shown in Fig. 5. The disturbance obtained from the PCC voltage through the

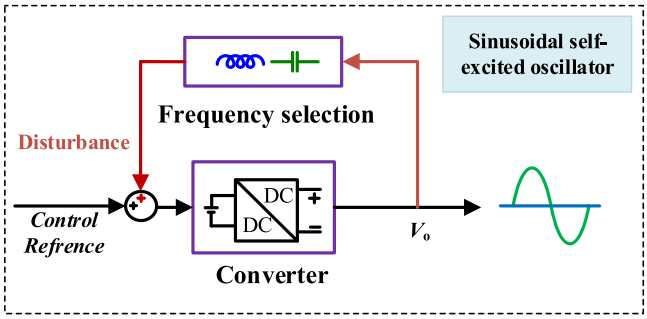

Fig. 5. Sinusoidal self-excited oscillator in power electronics.

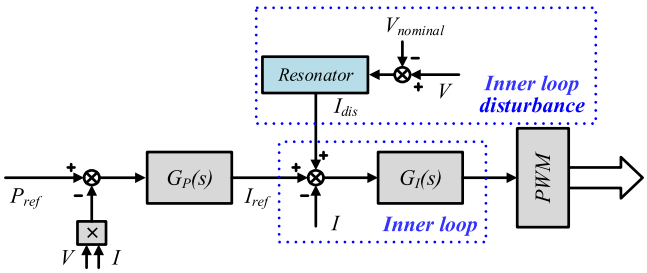

Fig. 6. Control diagram of proposed islanding detection with VPFOSF in inner loop.

frequency selection is added to the control reference of the converter to form the VPFOSF.

The amplitude and phase conditions shown in (12) and (13) should be both satisfied to achieve sinusoidal self-excited oscillation according to the control theory [29]. A resonant controller presented in (14) is chosen as the frequency selection since there is an enormous amplitude gain in the resonant angular frequency ($\omega_0 = 2\pi f_0$), which helps to satisfy the amplitude requirement of the oscillator (12) as well as the phase compensation in the resonant angular frequency where the phase quickly crosses from 90° to −90° helps to meet the phase requirement of the oscillator (13), as follows:

$$|A_C(f_0) \cdot A_F(f_0)| \geq 1 \tag{12}$$

$$\varphi_C(f_0) + \varphi_F(f_0) = 2n\pi \tag{13}$$

$$G_R = \frac{2K_r\omega_i s}{s^2 + 2\omega_i s + \omega_o^2}. \tag{14}$$

There are two schemes to realize a sinusoidal self-excited oscillator during the islanding mode in power electronics by disturbing the inner loop or outer loop reference. The inner loop scheme is adopted in this article to realize the proposed IDM because the most sensitive frequency of the PCC voltage to the current disturbance (60 Hz) is much higher than that of the power disturbance (0 Hz), and hence, the detecting speed of the inner loop scheme is faster than that of the outer loop scheme when the DG is equipped with the VPFOSF.

The control diagram of the inner loop disturbing scheme is given in Fig. 6. The deviation between the PCC voltage and the nominal voltage is sent to the resonator to obtain the current disturbance component. Then, the disturbing component is imposed on the reference command of the current control loop to constitute the VPFOSF. Since the construction of the voltage feedback loop is in the base control level of the DG, there is less added computation burden and operation time for microcontrollers.

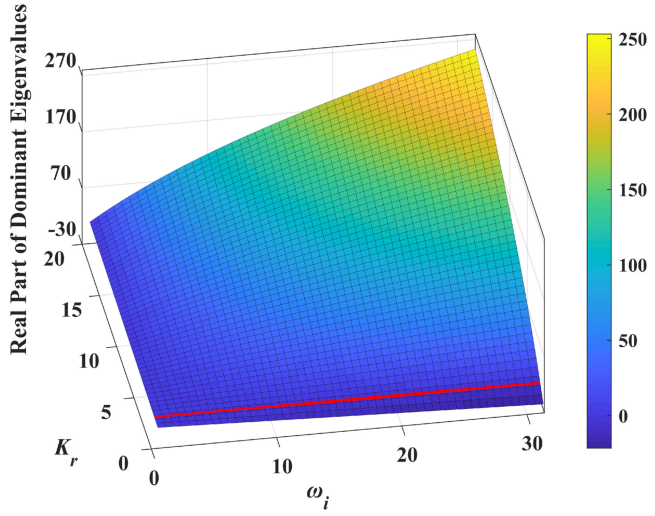

Fig. 7. Variation of real part of dominant eigenvalues during islanding condition with different combinations of K_r and ω_i when DG is equipped with VPFOSF in inner loop.

From the control diagram shown in Fig. 6, the characteristic equations of the PCC voltage during the islanding and grid-connected modes are given by

$$1 - G_R \cdot G_{In\_island} = 0 \tag{15}$$

$$1 - G_R \cdot G_{In\_grid} = 0. \tag{16}$$

The parameters of the resonator need to be designed to meet the two requirements making the PCC voltage oscillate at the selected frequency under the islanding condition but keep stable operation during the grid-connected mode. Then, the eigenvalue analysis is adopted to guide the parameter design in this article because the real part of the dominant eigenvalue can indicate the stability of the system and it is also positively correlated with the increasing rate of oscillating amplitude if the system is under an unstable state. Additionally, the frequency of oscillation is related to the imaginary part of the dominant eigenvalue.

The dominant eigenvalues of the system during the islanding mode and grid-connected mode are able to be calculated by (15) and (16), respectively. The variation of the real part of the dominant eigenvalues under the islanding condition with different combinations of K_r and ω_i is shown in Fig. 7 after the resonant frequency of resonator (f_0) is set to 45 Hz, whose detailed principle of selection is given in Section III. It is distinct that the real parts increase as the value of K_r rises from 0 to 20 and that of ω_i increases from 0 to 10π, which also means that the increasing rate of oscillating amplitude shall increase. The PCC voltage is under the critical stable state during the islanding mode if the values of K_r and ω_i are selected on the red line. The cases above the red line mean that the PCC voltage is under an unstable state. Similarly, the real parts of the dominant eigenvalues of the grid-connected condition which present the

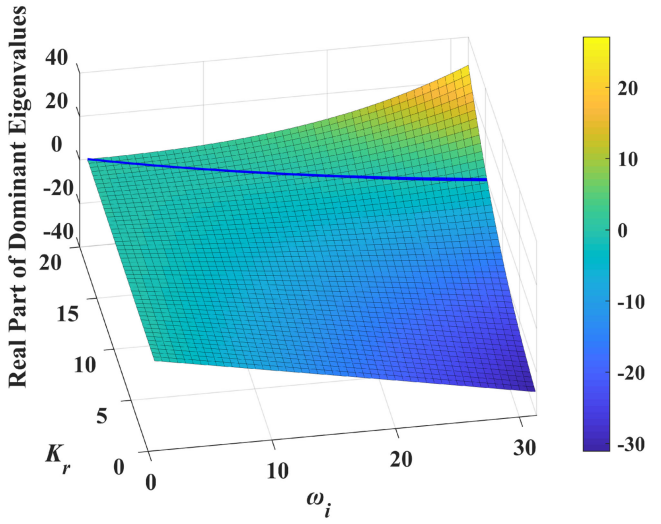

Fig. 8. Variation of real part of dominant eigenvalues during grid-connected condition with different combinations of K_r and ω_i when DG is equipped with VPFOSF in inner loop.

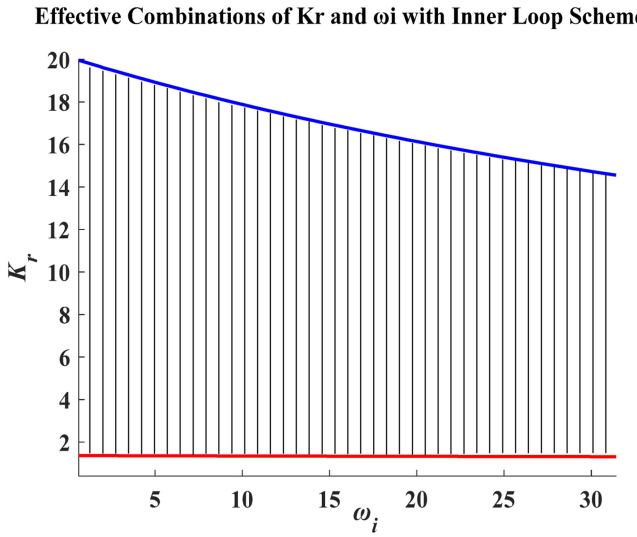

Fig. 9. Effective combinations of K_r and ω_i to realize the proposed islanding detection conception when DG is equipped with VPFOSF in inner loop.

same rising trend as that of the islanding condition with the value of K_r and ω_i increasing are displayed in Fig. 8. Fortunately, the value of K_r which makes the PCC voltage under the critical stable state during the gird-connected mode is much larger than that of the islanding case, as plotted in the blue line in Fig. 8. The cases under the blue line mean that the PCC voltage can remain stable. Then, the effective combinations of K_r and ω_i which make the PCC voltage oscillate under the islanding condition but keep stable during the grid-connected mode are between the two lines, as shown in the shaded area of Fig. 9. It can be seen that the range of effective K_r declines slowly with ω_i increasing.

The variation of the frequency of the dominant eigenvalues with the effective combinations of K_r and ω_i changing is presented in Fig. 10. The frequency is transferred from angular frequency divided by 2π for a better description. It can be

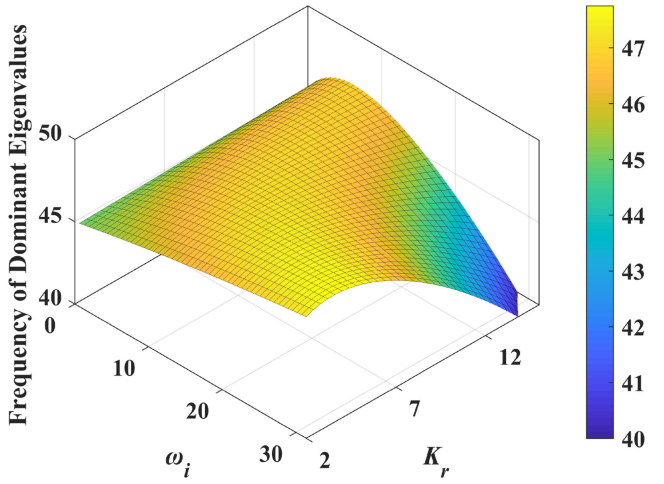

Fig. 10. Variation of frequency of dominant eigenvalues during islanding condition with different effective combinations of K_r and ω_i when DG is equipped with VPFOSF in inner loop.

seen that the analytical frequency in most cases is close to the set frequency of the resonator (45 Hz). It is worth noting that the deviation between the analytical frequency and set frequency could become large when the value of the real part of the dominant eigenvalue dramatically increases. However, the positive feedback path is only needed to make the real part of the dominant eigenvalue exceed a little more than the critical stability to guarantee the islanding detection during the islanding condition while also keeping enough stability margin during the grid-connected condition [25]. As a result, the practical frequency can be always designed close to the selected oscillating frequency (45 Hz) with little influence on the islanding detection.

III. Parameter Analysis and Performance Comparison

The selection of resonant frequency is presented in this section based on the consideration that enough stability margin should be ensured. Besides, it is also analyzed how K_r and ω_i influence the stability margin and the growth rate of oscillating amplitude at islanding events, which provides guidance for the resonator design. The comparison between islanding detection schemes with VPFOSF and VPFOFF is also given, and it indicates the advantage of attenuating the signal at the sensitive frequency band of the grid-connected condition.

A. Selection of Resonant Frequency

In order to simplify the analysis of the relationship between the stability margin and the set frequency of the resonator, it is assumed that the phase compensating function of the resonator can satisfy the phase requirement (13) at the set frequency under both the islanding condition and grid-connected condition, as shown in (17). This means that the stability margin is mainly determined by the magnitude margin

$$\varphi(G_R)\big|_{f_R} + \varphi(G_{In\_island/grid})\big|_{f_R} = 2n\pi. \qquad (17)$$

The stability of the PCC voltage under the islanding condition is set as the critical stable state just satisfying the amplitude

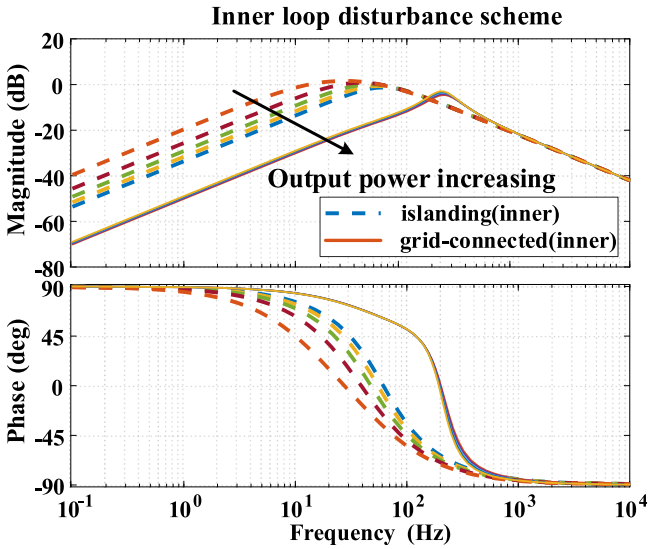

Fig. 11. Sensitivity of PCC voltage to current disturbance component with variation of output power of DG.

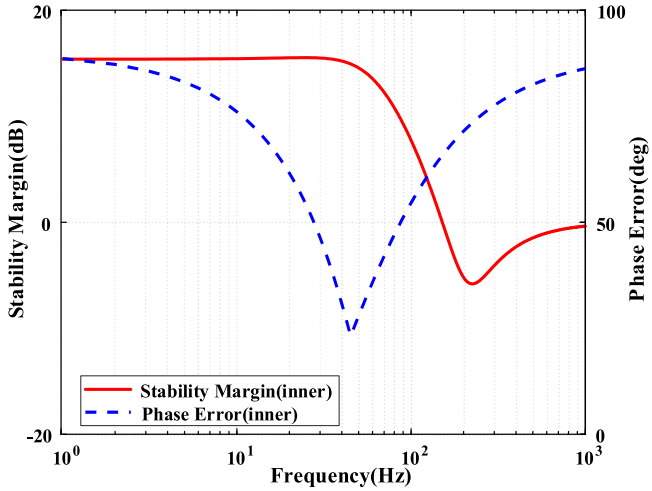

Fig. 12. Minimum stability margin during grid-connected mode and maximum phase error during islanding mode versus frequency when DG is equipped with VPFOSF in inner loop.

requirement for islanding detection. Then, the stability margin of the islanding mode can be given by

$$SM_{In\_island} = A(G_R)|_{f_R} + A(G_{In\_island})|_{f_R} = 0. \quad (18)$$

The magnitude is adopted in the logarithmic form to cater to the Bode plot. The stability margin of the PCC voltage under the grid-connected condition can be derived as

$$SM_{In\_grid} = 0 - (A(G_R)|_{f_R} + A(G_{In\_grid})|_{f_R}). \quad (19)$$

Substituting (18) into (19) yields

$$SM_{In\_grid} = A(G_{In\_island})|_{f_R} - A(G_{In\_grid})|_{f_R}. \quad (20)$$

Then, the stability margin of the PCC voltage under the grid-connected condition is determined by the difference in the sensitivity of the PCC voltage toward the disturbance component between the islanding and grid-connected modes.

The small-signal model can only be obtained under the determined parameters, but the parameters of the practical system may change under different operating conditions, such as the output power of the DG. The influence of the variation of the output power of the DG on the sensitivity of the PCC voltage to the current disturbance component is considered in Fig. 11, where the output power of DG varies from 20% of the rated power to 100%. All of them are under the condition where the power of generation and consumption is completely the same. It is clear that the sensitivity decreases during both modes with the output power increasing, and the variation rate of the islanding condition is much larger than that of the grid-connected mode.

Considering the implementation of the islanding detection under the hardest condition, the parameters (100% rated power) that make the PCC voltage the least sensitive to the current disturbance are adopted for calculating the islanding part of (20). The parameters (20% rated power) that make the PCC voltage the most sensitive to the current disturbance are adopted for calculating the grid-connected part of (20) to evaluate the stability margin of the worst case. Then, the stability margin under the grid-connected condition versus frequency when the DG is equipped with the VPFOSF in the inner loop is presented as the solid red line in Fig. 12 by calculating (20). It can be seen that the magnitude is much larger at the low-frequency band (under 60 Hz) where enough stability margin under the grid-connected condition can be ensured.

On top of that, the phase error that represents the maximum absolute value of the phase of the voltage sensitivity of the islanding mode (8) among all operating conditions versus frequency is obtained as the blue dotted lines of Fig. 12. The phase error which needs to be compensated by the resonator to meet the phase requirement (13) will increase the deviation between the practical frequency of oscillation and the set frequency of the resonator due to the nonideal resonator. Then, the frequency of the resonator when the inner loop being disturbed is set to 45 Hz since the phase error at 45 Hz is the minimum, and the stability margin is also enough.

B. Analysis of Resonator Parameters

Fig. 13 shows the dominant eigenvalue trajectory of the system with the K_r increasing from 2 to 8 when ω_i and f_0 are set to 2π and 45 Hz, respectively. It could be clearly seen that the growth rate of oscillating amplitude during the islanding mode sees an increase with K_r rising. The system stability under the grid-connected condition is studied by the Nyquist plots of the negative loop gain in the voltage loop ($-G_R G_{In\_grid}$) due to the positive feedback. The system stability can be determined by checking the number of encirclements around (-10) [30]. The stability margin decreases rapidly with the same K_r variation as before, as presented in Fig. 14.

The dominant eigenvalue trajectory of the system during the islanding mode with ω_i increasing from 2π to 12π is shown in Fig. 15 when K_r and f_0 are set to 2.5 and 45 Hz, respectively. It indicates that the growth rate of oscillating amplitude during the islanding mode rises rapidly as ω_i increases. The change of the system stability margin under the grid-connected condition can

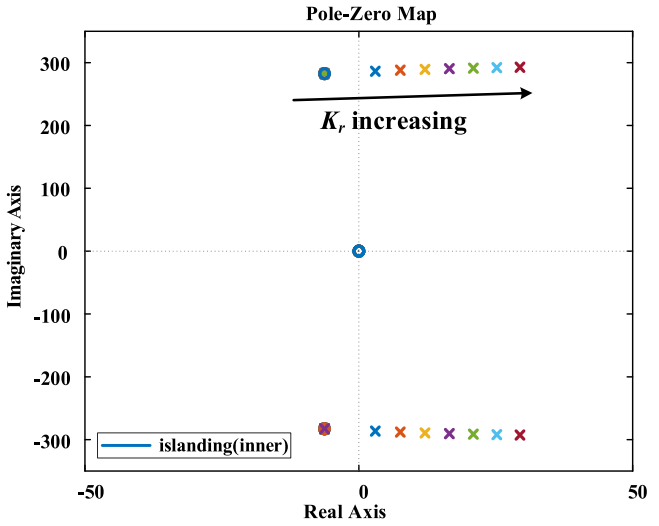

Fig. 13. Traces of system eigenvalues under islanding condition by varying K_r when DG is equipped with VPFOSF in inner loop.

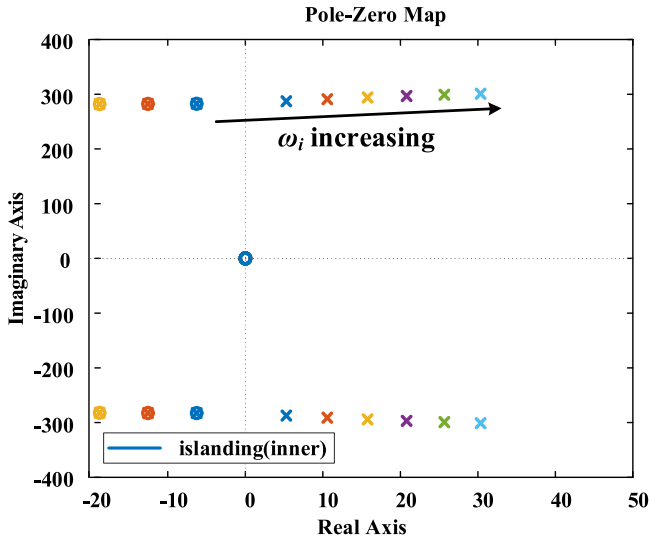

Fig. 15. Trace of the system eigenvalues under islanding condition by varying ω_i when DG is equipped with VPFOSF in inner loop.

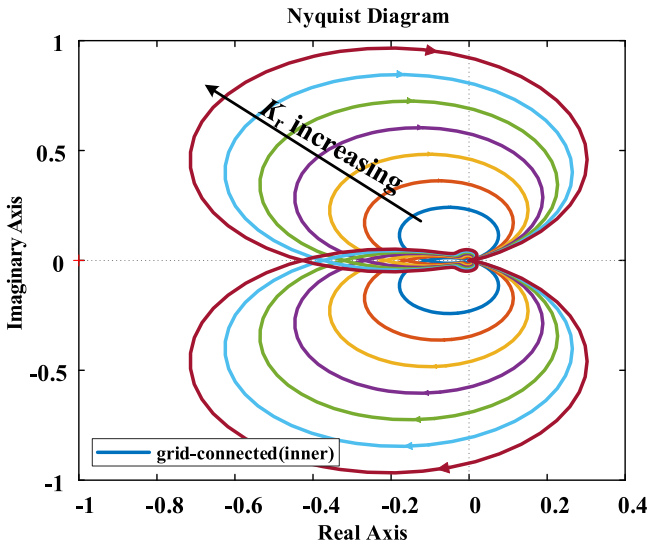

Fig. 14. Nyquist plots of negative loop gain in voltage loop under grid-connected condition by varying K_r when DG is equipped with VPFOSF in inner loop.

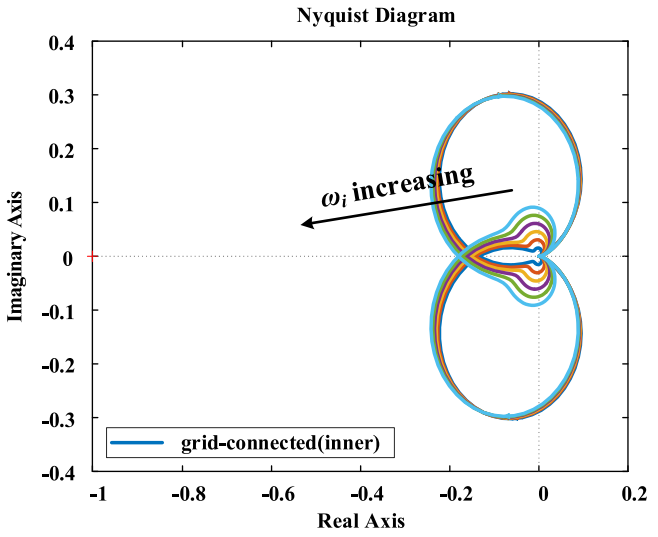

Fig. 16. Nyquist plots of negative loop gain in voltage loop under grid-connected condition by varying ω_i when DG is equipped with VPFOSF in inner loop.

be seen in Fig. 16 with the same ω_i change as before. The stability margin under the grid-connected condition is less influenced by the increase of ω_i from Fig. 16. This phenomenon can be furtherly analyzed by the Bode plot of the loop gain of the voltage loop under the islanding condition and grid-connected condition, as shown in Figs. 17 and 18, respectively. It can be seen that the maximum gain remains unchanged, but the bandwidth increases under the islanding condition with ω_i rising in Fig. 17. The magnitude stability margin under the grid-connected condition nearly stays the same with ω_i increasing in Fig. 18. Then, it can be concluded that increasing the bandwidth of the loop gain can improve the growth rate of oscillating amplitude with little influence on the stability margin. This contributes to designing the parameters of the resonator to obtain more stability margin under the grid-connected condition with identical oscillating speeds at islanding events.

C. Comparison Between Islanding Detection Schemes With VPFOSF and VPFOFF

The IDM with the VPFOFF in the inner loop does not consider the difference of the frequency where the PCC voltage is most sensitive to the current disturbance between the islanding condition and grid-connected condition. If the voltage feedback path is designed to pass the signal at the most sensitive frequency of the islanding condition and attenuate that of the grid-connected mode, the stability margin under the grid-connected condition can be improved without reducing the growth rate of oscillating amplitude at islanding events compared to the VPFOFF scheme. To validate the improvement of stability margin, the growth rate

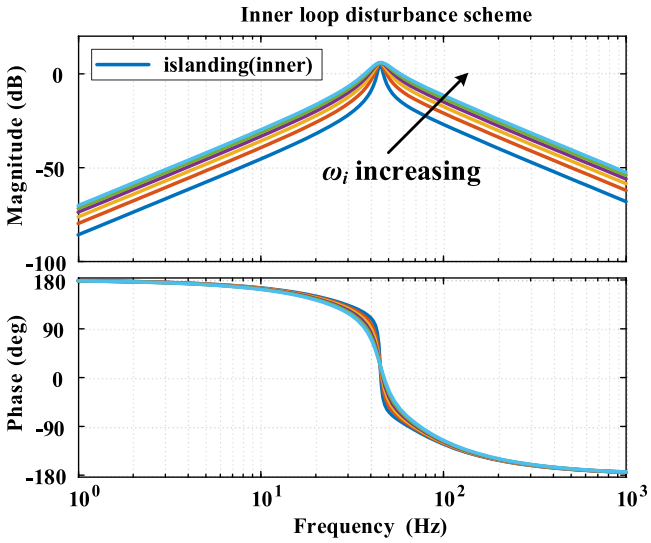

Fig. 17. Bode plots of loop gain in voltage loop under islanding condition by varying ω_i when DG is equipped with VPFOSF in inner loop.

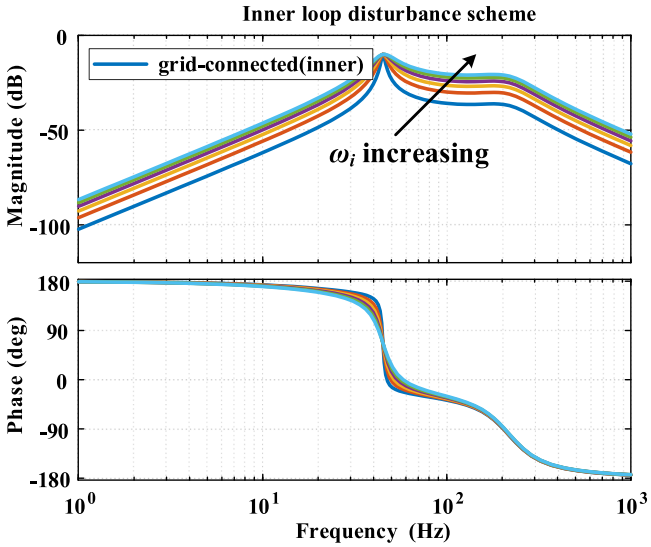

Fig. 18. Bode plots of loop gain in voltage loop under grid-connected condition by varying ω_i when DG is equipped with VPFOSF in inner loop.

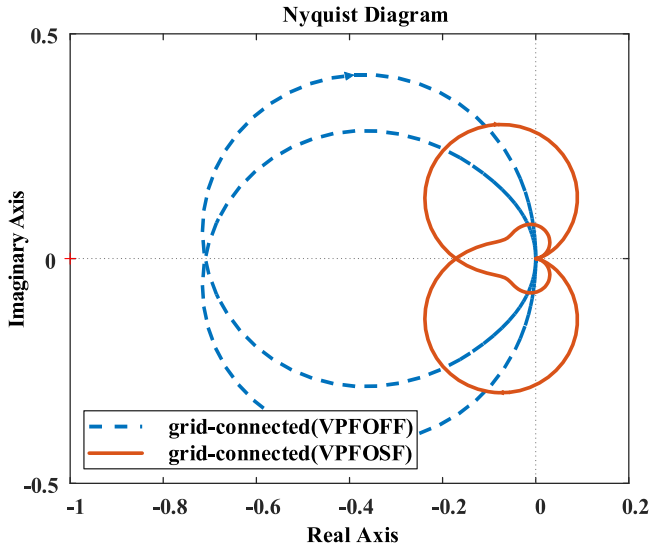

Fig. 19. Nyquist plots of negative loop gain in voltage loop when DG is equipped with VPFOSF and VPFOFF in inner loop, respectively.

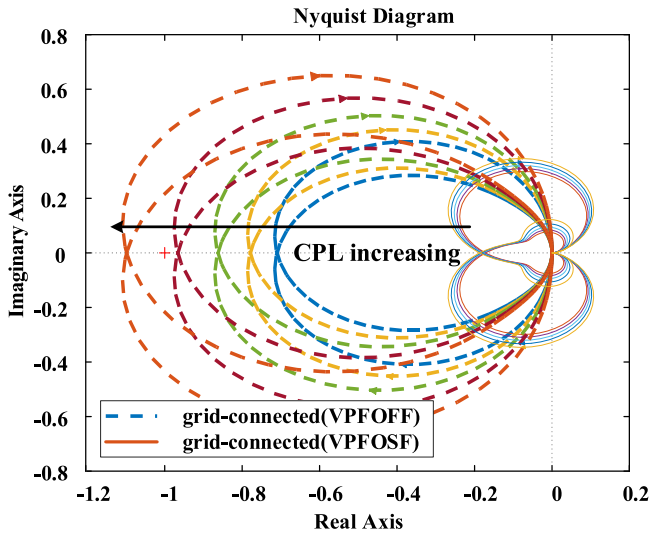

Fig. 20. Nyquist plots of negative loop gain in voltage loop by varying penetration of CPLs when DG is equipped with VPFOSF and VPFOFF in inner loop, respectively.

of the oscillating amplitude of the VPFOSF scheme is designed faster than that of the VPFOFF scheme, which is presented in Section V-D. Their stability margin under the grid-connected condition is presented in Fig. 19. It can be clearly seen that the magnitude margin of the VPFOSF scheme (15.29 dB) is much larger than that of the VPFOFF scheme (2.98 dB). This shows the advantage of the proposed VPFOSF in improving the stability margin with little impact on the islanding detection.

Furthermore, the impact of CPLs, which can deteriorate the stability of the systems, is studied in Fig. 20 [31]. The stability margin of the VPFOFF scheme reduces rapidly, with even unstable states appearing with the proportion of CPLs varying from 0% to 80%. However, the stability margin of the VPFOSF scheme is little influenced by the increase of the penetration of CPLs, because the frequency selection suppresses the signal at the most sensitive frequency of the grid-connected condition. This indicates the superiority of the VPFOSF scheme when the systems contain CPLs.

IV. Islanding Detection for Multiple-DG System

The proposed IDM is also investigated in multiple-DG systems. Multiple DGs connected in radial and bus configurations are common in dc microgrids, as shown in Fig. 21. It assumes that there are n DGs injecting current disturbances into their PCCs to detect the islanding condition in a multiple-DG system. The sensitivity matrix of PCCs voltage to the current disturbances under the grid-connected condition and islanding condition ($\boldsymbol{Z}_G$(s),

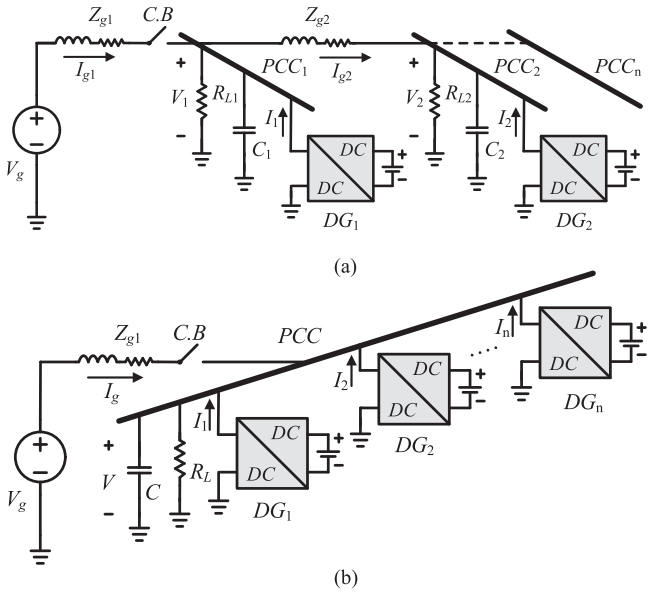

Fig. 21. Multiple-DG system configurations. (a) Multiple-DG system in a radial configuration. (b) Multiple-DG system in a bus configuration.

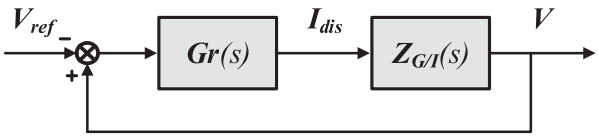

Fig. 22. Generic control diagram of VPFOSF.

$\boldsymbol{Z_I}$(s)) can be obtained from the small-signal model of the system during the two modes, respectively

$$\boldsymbol{Z_{G/I}}(s) = \tilde{\boldsymbol{V}}\left(\tilde{\boldsymbol{I}}_{\boldsymbol{dis}}\right)^{-1} \tag{21}$$

where $\tilde{\boldsymbol{V}}$ is the PCC voltage vector of dimension [$n\times1$], $\tilde{\boldsymbol{I}}_{\boldsymbol{dis}}$ is the current disturbance vector of dimension [$n\times1$], and matrix $\boldsymbol{Z_{G/I}}(s)$ is of dimension [$n\times n$]. To constitute the VPFOSF, the deviations between the voltages of PCCs and their reference voltages multiply the resonators to obtain the current disturbances

$$\tilde{\boldsymbol{I}}_{\boldsymbol{dis}} = \boldsymbol{G_r}(s)\left(\tilde{\boldsymbol{V}} - \tilde{\boldsymbol{V}}_{\boldsymbol{ref}}\right)^T \tag{22}$$

where $\boldsymbol{G_r}(s)$ is resonator vector of dimension [$n\times1$] and $\tilde{\boldsymbol{V}}_{\boldsymbol{ref}}$ is the PCC voltage reference vector of dimension [$n\times1$]. According to (21) and (22), the generic control diagram of VPFOSF is shown in Fig. 22.

From the control diagram, the closed-loop characteristic polynomial of the system under the grid-connected and islanding conditions can be obtained as

$$\det\boldsymbol{T_c}(s) = \det\boldsymbol{T_o}(s)\det(\boldsymbol{I_n} - \boldsymbol{G_r}(s)\boldsymbol{Z_{G/I}}(s)) \tag{23}$$

where $\boldsymbol{T_o}$(s) represents the open-loop characteristic polynomial of the system which has no zeros in the right-hand side of the s-plane and $\boldsymbol{I_n}$ is the identity matrix of dimension [$n\times n$]. Furthermore, the stability of the system under the two conditions depends on

$$SE_{G/I} = \det(\boldsymbol{I_n} - \boldsymbol{G_r}(s)\boldsymbol{Z_{G/I}}(s)). \tag{24}$$

If $SE_{G/I}$ have zeros (eigenvalues) on the right-hand side of the s-plane, the system is unstable. In order to implement the proposed islanding detection conception that the PCCs voltages appear to oscillate at the selected frequency in the case of islanding but remain stable during the grid-connected mode, the parameters of $\boldsymbol{G_r}(s)$ vector should be designed to make SE_I have zeros in the right-hand side of the s-plane but make SE_G have no zeros on the right-hand side of the s-plane.

First, according to the PCCs voltage sensitivity matrix and the mentioned design principle in Section III, the appropriately oscillated frequency (f_0) of each DG can be determined. To share the contribution to the oscillation of each DG at the islanding events and simplify the design of parameters of the $\boldsymbol{G_r}(s)$ vector, the loop gain of positive voltage feedback of each DG at the selected oscillating frequency is assigned to be equal, as shown in (25), and the resonator bandwidth of each DG is also assigned to the same as presented in (26). Then, the methodology of K_r, ω_i design in the single-DG system can be applied to the multiple-DG system by variable substitution

$$K_{r1}\,Z_{I_{11}}|_{f_{01}} = K_{r2}\,Z_{I_{22}}|_{f_{02}} \cdots = K_{rn}\,Z_{I_{nn}}|_{f_{0n}} \tag{25}$$

$$\omega_{i1} = \omega_{i2} \cdots = \omega_{in}. \tag{26}$$

An example consisting of two DGs connected in a radial configuration shown in Fig. 21(a) is adopted to validate the proposed IDM since the bus configuration is the particular case of the counterpart. Another DG which is accompanied by two times the conductor and bus capacitance than the single DG is added to form the multiple-DG system. Its parameters are shown in No. 2 parameters of simulation in Table I. The sensitivity matrix of the system is obtained with the help of the small-signal model and verified by a nonlinear model in Simulink, as shown in the Appendix. The selected oscillating frequencies of the two DGs are set to 45 Hz. Combined with (24)–(26), the variations of the real part of dominant eigenvalues of the system under the islanding condition and grid-connected condition with K_{r1} and ω_{i1} changing are presented in Figs. 23 and 24, respectively. The red and black lines represent the combinations of K_{r1} and ω_{i1} which can make the islanding and grid-connected system under the critical stable state, respectively. The combinations of K_{r1} and ω_{i1} between the red and black lines can make PCCs voltage oscillate at the selected frequency in the case of islanding but stay stable under the grid-connected condition to implement the proposed islanding detection conception.

V. Simulation Results

The proposed islanding detection scheme is evaluated in the MATLAB/Simulink environment to study their effectiveness when the DG shown in Fig. 1 is equipped with it. There are two approaches to indicate islanding events. One is that the under/overvoltage protection is set to operate between 0.88 and 1.1 p.u., out of which means the islanding condition. Another way proposed in this article is that a divergent voltage oscillation

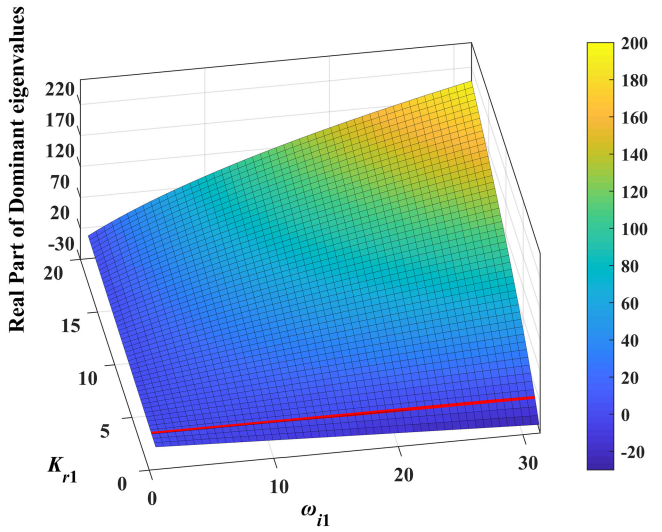

Fig. 23. Variation of real part of dominant eigenvalues under islanding condition with different combinations of K_{r1} and ω_{i1} when DGs are equipped with VPFOSF in inner loop.

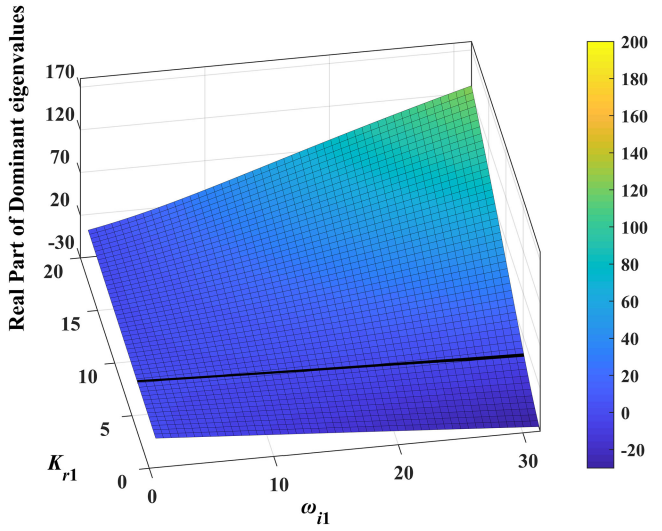

Fig. 24. Variation of real part of dominant eigenvalues under grid-connected condition with different combinations of K_{r1} and ω_{i1} when DGs are equipped with VPFOSF in inner loop.

of three continuous cycles whose oscillating frequency is at the preconcerted range indicates the islanding event. The range in this article is set to $f_0 \pm 5$ Hz (40, 50 Hz). The dc system simulation parameters are shown in Table I. The solver in Simulink is selected as ode45. The relative and absolute tolerances are set to 10^{-12} and 10^{-96}, respectively.

A. Single-DG System

When the power of generation agrees with that of consumption and the load is purely resistive, this is the hardest condition for islanding detection. Then, this case is first evaluated to show the whole process of the islanding detection utilizing the frequency information. K_r, ω_i, and f_0 are set to 2.5, 10π, and 45 Hz, respectively, in the single-DG system simulations. The

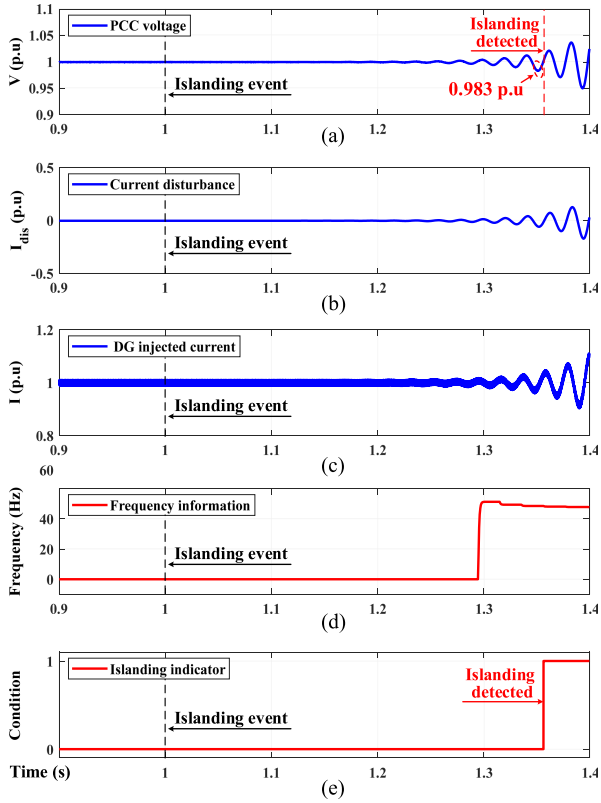

Fig. 25. System response at an islanding event when DG is equipped with VPFOSF.

practical islanding event is set to take place at time $t = 1$ s. The DG and the load are set to the rated power in this case. It can be clearly seen that there is no PCC voltage fluctuation when the island occurs at first due to the match between the power of consumption and generation. But the voltage gradually oscillates at the frequency which tends to be 47 Hz, as presented in Fig. 25(a) and (d), because of the loss of the voltage regulation. The disturbance component of the current is plotted in Fig. 25(b). It is close to zero under the grid-connected condition and forms the mutual excitation with the PCC voltage after the islanding event. The current disturbance results in the change of the current, as indicated in Fig. 25(c). The islanding indicator detects the event at 1.351 s, as presented in Fig. 25(e). And it can be seen that the PCC voltage fluctuation is less than 0.02 p.u. when the islanding event is detected. The proposed scheme satisfies the requirement of the islanding detection time of under 2 s [19]. In the meanwhile, it has the advantage of less voltage fluctuation.

The stable boundaries under the islanding condition and grid-connected condition are also investigated. ω_i is set to 10π in this analytical case. Then, the theoretical $K_r s$ to make the system at the critical stable state under the islanding condition and grid-connected condition are 1.312 and 14.56, respectively, based on the derived model. The voltage oscillations with the constant amplitude after a small disturbance are shown in Fig. 26, when $K_r s$ are set to 1.308 and 14.335 under the islanding condition and grid-connected condition, respectively. This proves that the

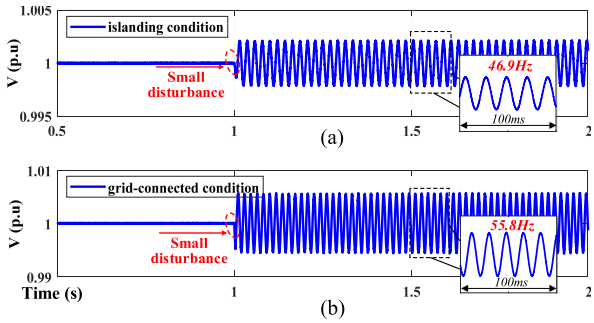

Fig. 26. Voltage response after a small disturbance when system is at critical stable state under islanding and grid-connected conditions.

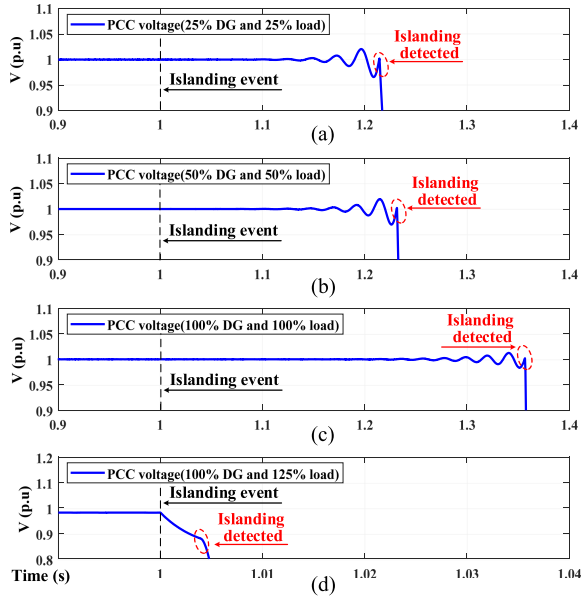

Fig. 27. Islanding tests for different power operating conditions when DG is equipped with VPFOSF.

practical stable boundaries agree with those of the theoretical analysis.

B. Test of Robustness of Proposed IDM

1) Effectiveness of Proposed IDM at Different Power Conditions: The four different operating conditions under which the DG and load both operate at 25%, 50%, 100% of the rated power, as well as the DG and the load work at 100% and 125% of the rated power, respectively, need to be considered for testing the proposed islanding detection scheme from IEEE standard [19]. The simulation results when the DG is equipped with VPFOSF are presented in Fig. 27. It is clearly seen that the islanding event under all operating conditions can be detected within 2 s. The DG stops energizing the load after the islanding events being detected. The islanding events under the three operating conditions where the power of consumption and generation is fully the same can be detected quickly with less voltage fluctuation by frequency information, as displayed in Fig. 27(a)–(c). The detecting time increases with the system power rising, which is coincident with the previous sensitivity analysis when the

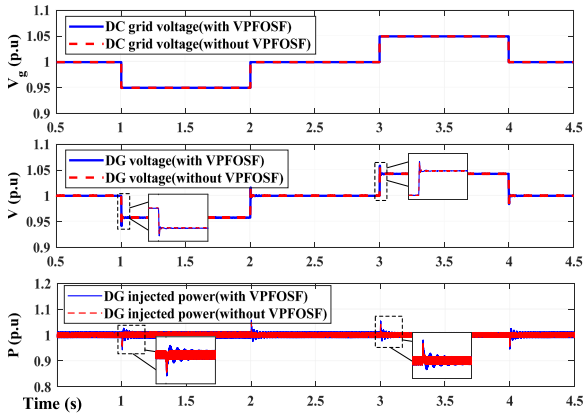

Fig. 28. Output power response with dc grid voltage changing when DG is equipped with and without VPFOSF.

DG injected power varies. On top of that, the voltage under the power mismatching condition is shifted out of the normal range during one oscillating period to indicate the islanding event, as presented in the case in Fig. 27(d). These cases indicate that the combination of passive IDMs and active IDMs is a more practical way to eliminate the nondetecting zone and implement quick islanding detection.

2) Impact of DC Grid Voltage Changing: The variation of the dc grid voltage under the grid-connected condition needs to be considered to evaluate the robustness of the proposed IDM. The simulation results that the dc gird voltage varies by $\pm 5\%$ of the nominal voltage are shown in Fig. 28 when the DG is equipped with and without the proposed scheme. It is distinctly noticed that the output power of the DG remains unchanged at the steady state as 0 Hz is attenuated by the resonator, and the dynamics of PCC voltage at the two cases are nearly the same. This shows the good robustness of the proposed scheme while the dc grid voltage changes.

3) Impact of Power Changing Including DG Injected Power and Load Consumption: The power changing in the dc systems is one of the main factors causing PCC voltage fluctuation. Then, the impact of variations of DG injected power and load consumption on the PCC voltage when the DG is equipped with and without VPFOSF are simulated, as shown in Fig. 29. The DG injected power varies by $+10\%$, -10% at 0.5 and 1.5 s, respectively. The resistive load decreases by 10% at 2.5 s and increases by 10% at 3.5 s. From the comparison between the conditions with the proposed IDM and without that, they are nearly the same in terms of the impact on PCC voltage when the power changes.

The disturbances during the normal condition would cause PCC voltage fluctuation but the amplitude of the voltage fluctuation would persistently decline due to the existence of voltage regulation. As a result, these disturbances would not cause fault detection.

C. Seamless Transfer After Islanding Event

In terms of some critical loads, the control target of some DGs needs to be transferred from the power control to the voltage

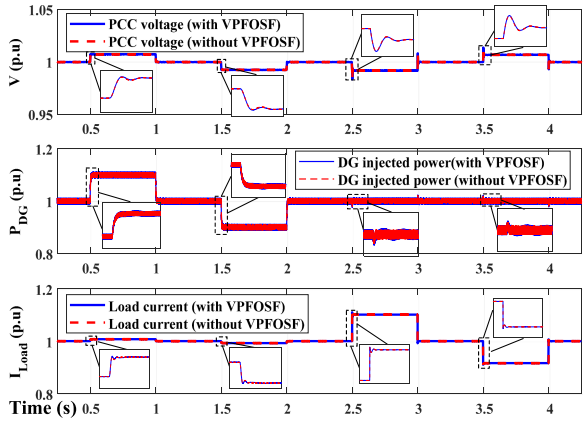

Fig. 29. System response with DG injected power and load changing when DG is equipped with and without VPFOSF.

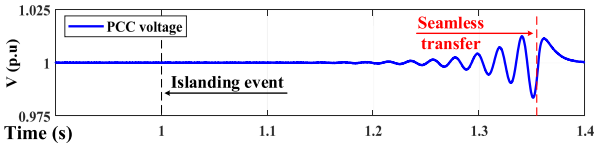

Fig. 30. Seamless transfer after islanding event when DG is equipped with VPFOSF.

regulation to improve the power supply reliability [32]. Once the islanding event is detected, the outer loop control switches from the power control to the voltage regulation whose control bandwidth is set to 240 Hz. The whole process from the islanding event to finishing seamless transfer is plotted in Fig. 30. It can be clearly seen that the voltage recovers smoothly back to the nominal value after the islanding condition is detected since there is only a very small voltage fluctuation (<0.02 p.u.) when the islanding event is detected by utilizing the frequency information.

D. Impact on Detecting Speed and Stability Margin With K_r and ω_i Increasing

As mentioned in the previous analysis, increasing K_r could enhance the islanding detecting speed and extremely decrease the stability margin under the grid-connected condition, but the rising of ω_i can improve the islanding detecting speed with less impact on the stability margin under the grid-connected condition. To validate the conclusion, the variation trends of detecting time and stability margin with the change of K_r and ω_i are obtained by simulation results, as shown in Figs. 31 and 32. The stability margin is represented by the proportion of CPL to make the system at the critical stable. When increasing K_r to reduce the detecting time by about 50%, the stability margin decreases by about 80%. However, the stability margin reduces by only 15% while the detecting time declines by about 50% with ω_i rising. The simulation results completely agree with the theoretical analysis.

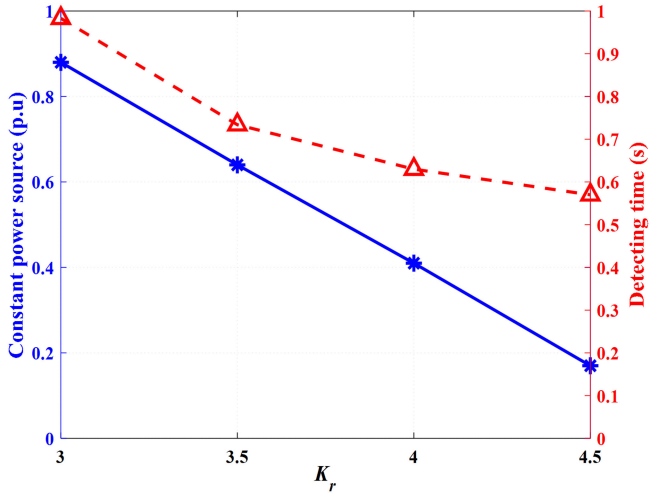

Fig. 31. Variation trends of constant power source and detecting time with K_r increasing.

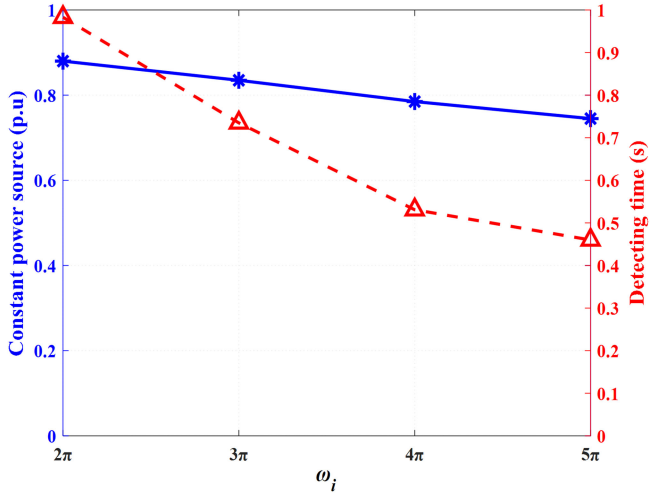

Fig. 32. Variation trends of constant power source and detecting time with ω_i increasing.

E. Comparison Between Islanding Detection Schemes With VPFOSF and VPFOFF

In order to validate the advantage of VPFOSF improving the stability margin under the grid-connected condition, the VPFOSF scheme is designed to have a much higher growth rate of oscillating amplitude than the VPFOFF scheme, since the growth rate of oscillating amplitude and stability margin are opposite. The former uses the same parameters as before, and the positive feedback gain of the latter is set to 1.22.

Then, the growth rate of the oscillating amplitude of the VPFOSF scheme is much higher than that of the VPFOFF, as shown in Fig. 33(a). The load consisting of CPL and resistive load is adopted to evaluate the stability margin. The CPL and resistive load account for 90% and 10% of the rated power, respectively. The PCC voltage begins to oscillate under the grid-connected condition when the VPFOFF scheme is enabled at 1 s, as shown in Fig. 33(b). However, when the detecting scheme switches to the VPFOSF at 2 s, the oscillation of the PCC voltage disappears.

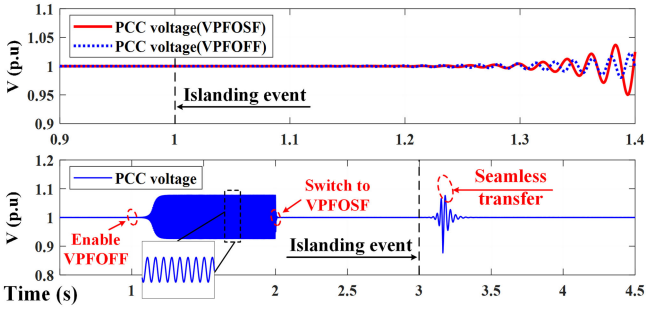

Fig. 33. System response when DG is equipped with VPFOFF and VPFOSF scheme, respectively.

On top of that, the islanding event occurring at 3 s is detected successfully after 167 ms. It concludes that the stability margin of the VPFOSF scheme outdistances that of the VPFOFF and suffers less from the impact of CPLs, which is coincident with the previous theoretical analysis in Section III-C.

F. Multiple-DG System

Several simulations are carried out to verify the effectiveness of the proposed IDM in the multiple-DG system with the radial configuration, as shown in Fig. 21(a). The simulation parameters are shown in Table I. K_{r1} and K_{r2} are set to 3 and 3.037, respectively. ω_{i1} and ω_{i2} are both selected as 5π. f_{01} and f_{02} are both set to 45 Hz. The system responses with different power conditions are shown in Fig. 34 when the islanding event happens at 1 s. When the DGs and loads are the rated power, the successful islanding detection costs almost 700 ms, as shown in the cases in Fig. 34(a) and (b). When DG_2 and $load_2$ are only half of the rated power, the detecting time decreases to 585 ms, as presented in the cases in Fig. 34(c) and (d), which proves the former analysis that the decline in the system power would increase the sensitivity of the PCC voltage to the disturbance. The cases in Fig. 34(e) and (f) in which the power generation and consumption at each PCC are not the same but the two of the whole system are almost equal also validate the effectiveness of the proposed IDM. It shows a faster detecting speed than the other cases since the power exchange of PCCs leads to a little deviation between the PCC voltage and nominal value under the grid-connected condition.

VI. Experimental Validation

To validate the performance of the presented islanding detection scheme, a lab-scale system is adopted, as shown in Fig. 35. A buck-converter is employed as a DG unit to energize a resistive load, as presented in Fig. 1. A fixed dc source is used as the dc grid to regulate the PCC voltage. The parameters of the experimental platform are given in Table I.

The set frequency of the resonator (f_0) is selected as 25 Hz since this is the appropriate frequency in terms of the experiment parameters. The power generation and consumption are set equal to verify the hardest condition for islanding detection. The system response after an islanding event in the single-DG system is shown in Fig. 36. The islanding event is created by

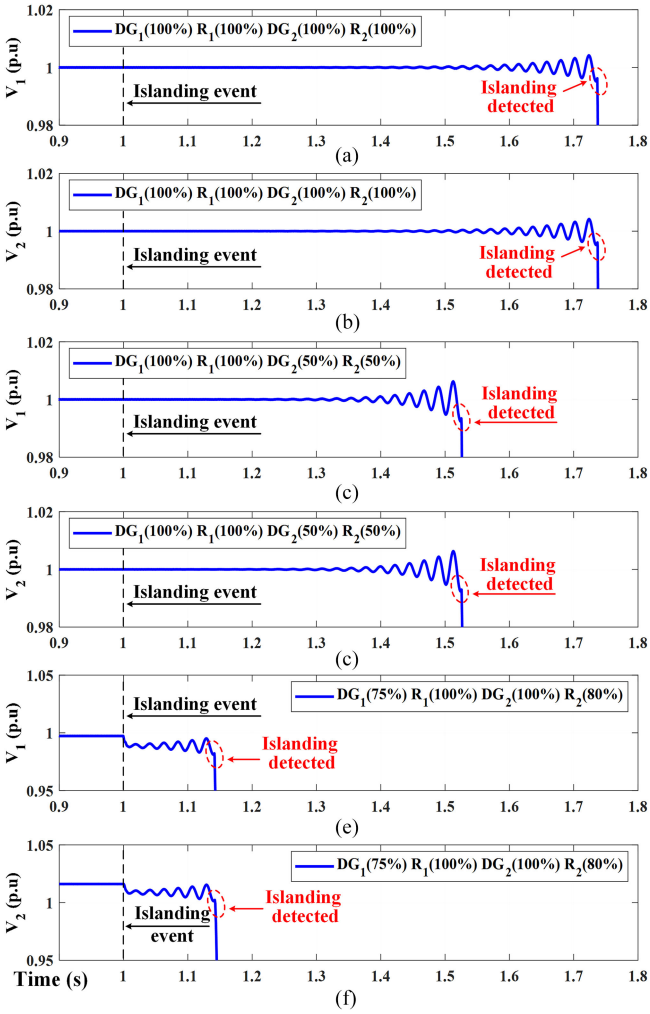

Fig. 34. System response after an islanding event with different power conditions in multiple-DG system.

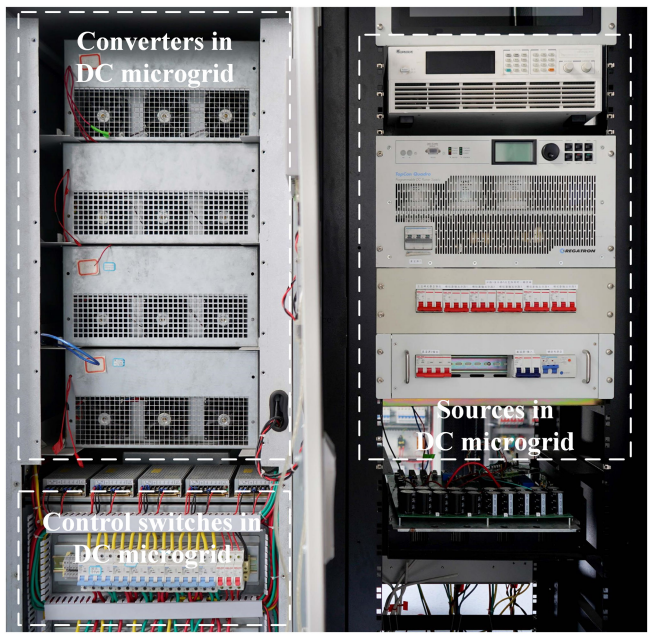

Fig. 35. Experimental platform of dc microgrid.

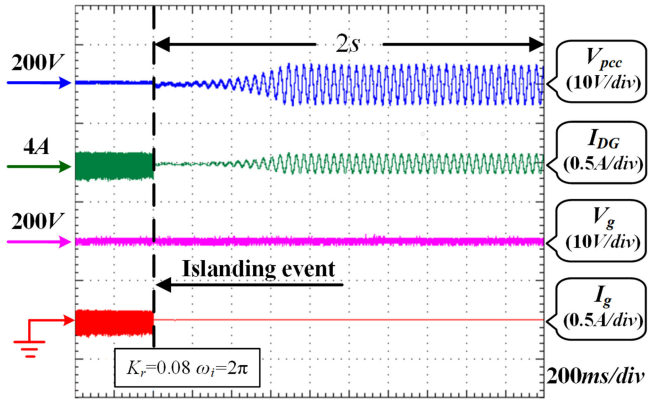

Fig. 36. System response at an islanding event in single-DG system.

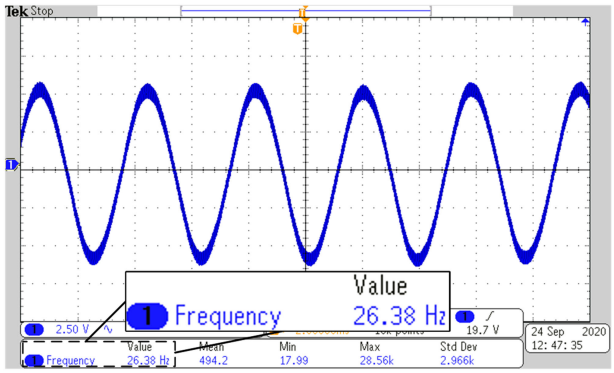

Fig. 37. AC component of voltage oscillation at an islanding event.

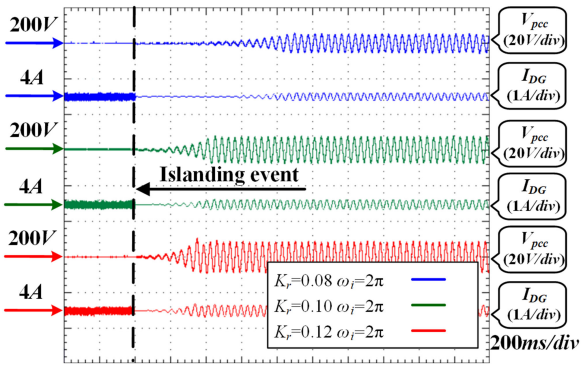

Fig. 38. Voltage responses with K_r rising at an islanding event.

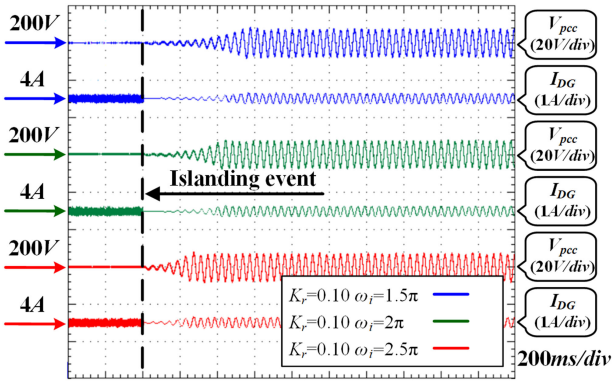

Fig. 39. Voltage responses with ω_i rising at an islanding event.

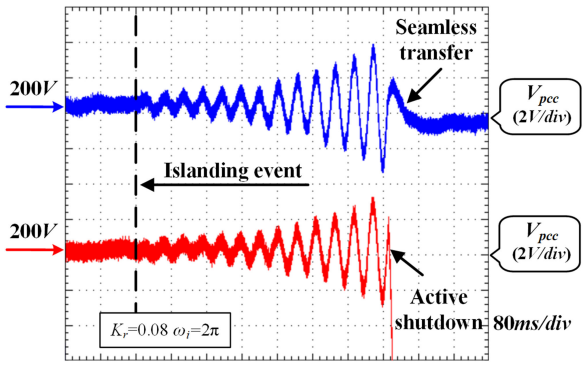

Fig. 40. Seamless transfer and active shutdown after an islanding event being detected.

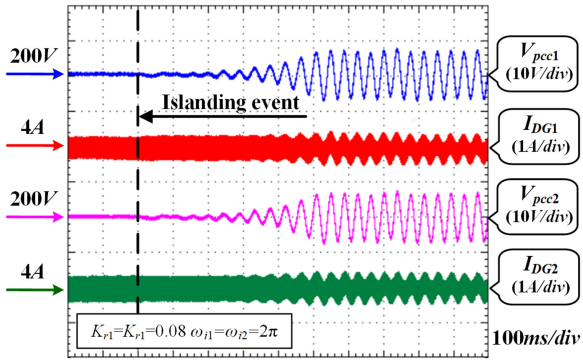

Fig. 41. System response at an islanding event in multiple-DG system.

manually disconnecting the switch between the dc grid and the PCC. When the islanding event occurs, the switching ripple of the DG injected current decreases to few since the equivalent impedance seen from the DG converter under the grid-connected condition is much smaller than that of the islanding condition, and the dc grid current becomes zero due to the disconnection between the voltage regulation converter and the PCC. Besides, the voltage oscillation whose frequency is close to the set value gradually occurs to indicate the islanding event. The zoom of the PCC voltage oscillation waveform is presented in Fig. 37. The practical frequency of voltage oscillation is 26.38 Hz, which agrees with the theoretical frequency (25 Hz).

The impacts of variations of K_r and ω_i on the growth rate of oscillating amplitude are shown in Figs. 38 and 39, respectively. It can be concluded that the growth rate of oscillating amplitude increases with K_r and ω_i rising, which corresponds with the previous theoretical analysis results. The system operations, including seamless transfer and active shutdown, are shown in Fig. 40 after an islanding event being detected. The application of the proposed IDM in a system with the same two DGs in bus configuration is presented in Fig. 41. The voltage oscillation in the selected frequency after the islanding event validates the effectiveness of the proposed IDM in the multiple-DG system.

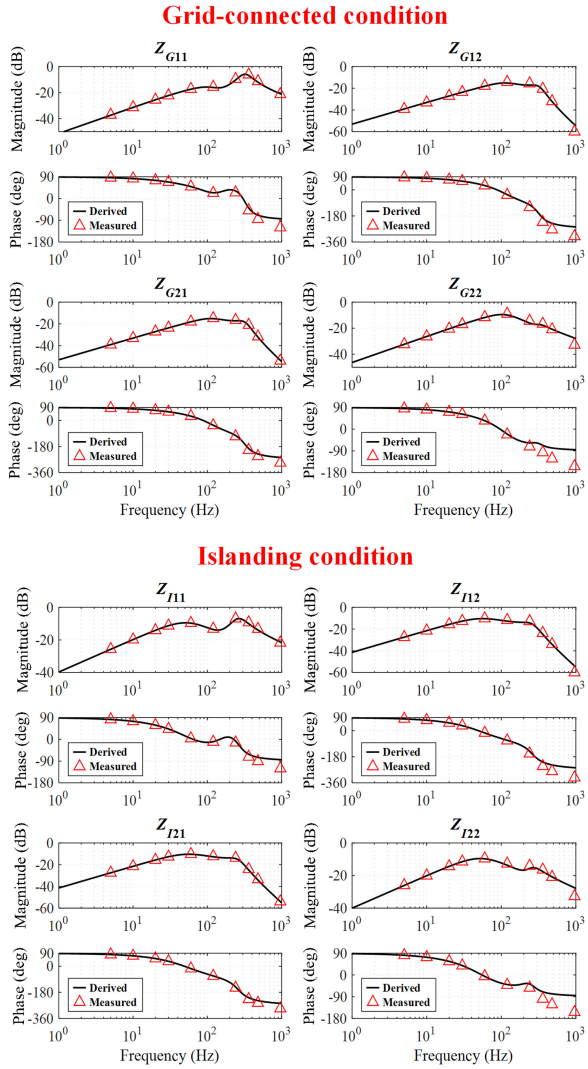

Fig. 42. Frequency response of sensitivity matrix of PCC voltage to current disturbance.

VII. Conclusion

A dc-based islanding detection scheme taking advantage of frequency information of the voltage oscillation at an islanding event was presented in this article. First, the sensitivity of the PCC voltage to disturbances in the frequency domain was investigated. It showed that the low-frequency band was more suitable for disturbance, and the most sensitive frequency bands to the current disturbance under the islanding and grid-connected conditions were different. Then, a DG combined with a resonator to construct the voltage positive feedback of selected frequency was presented to implement the proposed IDM. Besides, the design of the resonator and its influence on detecting speed and stability margin were studied. It was found that the detecting speed can be improved with little influence on the stability margin by increasing the bandwidth of the voltage feedback loop, and the stability margin of the grid-connected condition could be enhanced without influencing the islanding detection by attenuating the most sensitive frequency band of the grid-connected condition when the VPFOSF is adopted in the inner loop. Moreover, the application and design of the proposed IDM in multiple-DG system was presented. Finally, the detailed implementation with the simulation in MATLAB/Simulink and experiment from the laboratory dc system verified the effectiveness and theoretical analysis of the proposed strategy.

Appendix

A. Sensitivity Matrix of PCC Voltage to Current Disturbance Derivation in Multiple-DG System

Two DGs connected in the radial configuration are demonstrated as a design example, as shown in Fig. 21(a). The model is linearized at the power matching condition at each PCC, which is the hardest case for islanding detection. Then, the loop voltage and nodal current equations under the grid-connected and islanding conditions can be given by

$$\begin{cases} Z_{g1}\tilde{I}_{g1}+\tilde{V}_1=\tilde{V}_g, \tilde{I}_{g1}+\tilde{I}_1=Y_1\tilde{V}_1+\tilde{I}_{g2}(\text{Grid}-\text{con.}) \\ \tilde{I}_1=Y_1\tilde{V}_1+\tilde{I}_{g2}(\text{Islanding}) \end{cases}$$
$$\mathrm{Z}_{g2}\tilde{I}_{g2}+\tilde{V}_2=\tilde{V}_1, \tilde{I}_{g2}+\tilde{I}_2=Y_2\tilde{V}_2$$
$$\mathrm{Z}_{g1}=sL_{g1}+R_{g1}, \mathrm{Z}_{g2}=sL_{g2}+R_{g2}$$
$$Y_1=sC_1+\frac{1}{R_{L1}}, Y_2=sC_2+\frac{1}{R_{L2}}. \tag{27}$$

The control equations of each DG can be given by

$$\tilde{I}_{ref1}=G_p\left(\tilde{P}_{ref1}-\tilde{P}_1\right), \tilde{I}_{ref2}=G_p\left(\tilde{P}_{ref2}-\tilde{P}_2\right)$$
$$\tilde{I}_1=\tilde{I}_{ref1}+\tilde{I}_{dis1}, \tilde{I}_2=\tilde{I}_{ref2}+\tilde{I}_{dis2}$$
$$\tilde{P}_1=I_{o1}\tilde{V}_1+V_{o1}\tilde{I}_1, \tilde{P}_2=I_{o2}\tilde{V}_2+V_{o2}\tilde{I}_2$$
$$G_p=K_{pp}+K_{pi}/s. \tag{28}$$

The variation of the references of power loop $\tilde{P}_{\text{ref1}}$ and $\tilde{P}_{\text{ref2}}$ are set to zero while investigating the impact of the disturbance components. Solving (27) and (28) under the grid-connected and islanding conditions, respectively, the sensitivity matrix during the two modes can be given by

$$\mathrm{Z}_G=\begin{bmatrix} Z_{G11} & Z_{G12} \\ Z_{G21} & Z_{G22} \end{bmatrix}=\begin{bmatrix} \frac{n_{G11}}{d_G} & \frac{n_{G12}}{d_G} \\ \frac{n_{G21}}{d_G} & \frac{n_{G22}}{d_G} \end{bmatrix}$$
$$n_{G11}=Z_{g1}+G_pV_{o2}Z_{g1}+G_pI_{o2}Z_{g2}Z_{g1}+Y_2Z_{g2}Z_{g1}$$
$$+G_pV_{o2}Y_2Z_{g2}Z_{g1}, n_{G12}=Z_{g1}+G_pV_{o1}Z_{g1}$$
$$n_{G21}=Z_{g1}+G_pV_{o2}Z_{g1}, n_{G22}=Z_{g2}+G_pV_{o1}Z_{g2}+Z_{g1}$$
$$+G_pV_{o1}Z_{g1}+G_pI_{o1}Z_{g2}Z_{g1}+Y_1Z_{g2}Z_{g1}+G_pV_{o1}Y_1Z_{g2}Z_{g1}$$
$$d_G=1+G_pV_{o1}+G_pV_{o2}+{G_p}^2V_{o1}V_{o2}+G_pI_{o2}Z_{g2}$$
$$+{G_p}^2I_{o2}V_{o1}Z_{g2}+Y_2Z_{g2}+G_pV_{o1}Y_2Z_{g2}+G_pV_{o2}Y_2Z_{g2}$$
$$+{G_p}^2V_{o1}V_{o2}Y_2Z_{g2}+G_pI_{o1}Z_{g1}+G_pI_{o2}Z_{g1}$$
$$+{G_p}^2I_{o2}V_{o1}Z_{g1}+{G_p}^2I_{o1}V_{o2}Z_{g1}+Y_1Z_{g1}+G_pV_{o1}Y_1Z_{g1}$$
$$+G_pV_{o2}Y_1Z_{g1}+{G_p}^2V_{o1}V_{o2}Y_1Z_{g1}+Y_2Z_{g1}+G_pV_{o1}Y_2Z_{g1}$$
$$+G_pV_{o2}Y_2Z_{g1}+{G_p}^2V_{o1}V_{o2}Y_2Z_{g1}+{G_p}^2I_{o1}I_{o2}Z_{g2}Z_{g1}$$
$$+G_pI_{o2}Y_1Z_{g2}Z_{g1}+{G_p}^2I_{o2}V_{o1}Y_1Z_{g2}Z_{g1}+G_pI_{o1}Y_2Z_{g2}Z_{g1}$$
$$+{G_p}^2I_{o1}V_{o2}Y_2Z_{g2}Z_{g1}+Y_1Y_2Z_{g2}Z_{g1}+G_pV_{o1}Y_1Y_2Z_{g2}Z_{g1}$$
$$+G_pV_{o2}Y_1Y_2Z_{g2}Z_{g1}+{G_p}^2V_{o1}V_{o2}Y_1Y_2Z_{g2}Z_{g1} \tag{29}$$

$$
\begin{aligned}
&\mathrm{Z}_I = \begin{bmatrix} Z_{I11} & Z_{I12} \\ Z_{I21} & Z_{I22} \end{bmatrix} = \begin{bmatrix} \frac{n_{I11}}{d_I} & \frac{n_{I12}}{d_I} \\ \frac{n_{I21}}{d_I} & \frac{n_{I22}}{d_I} \end{bmatrix} \\
&n_{I11} = 1 + G_p V_{o2} + G_p I_{o2} Z_{g2} + Y_2 Z_{g2} + G_p V_{o2} Y_2 Z_{g2} \\
&n_{I12} = 1 + G_p V_{o1}, n_{I21} = 1 + G_p V_{o2}, n_{I22} = 1 + G_p V_{o1} \\
&+ G_p I_{o1} Z_{g2} + Y_1 Z_{g2} + G_p V_{o1} Y_1 Z_{g2} \\
&d_I = G_p I_{o1} + G_p I_{o2} + {G_p}^2 I_{o2} V_{o1} + {G_p}^2 I_{o1} V_{o2} + Y_1 \\
&+ G_p V_{o1} Y_1 + G_p V_{o2} Y_1 + {G_p}^2 V_{o1} V_{o2} Y_1 + Y_2 + G_p V_{o1} Y_2 \\
&+ G_p V_{o2} Y_2 + {G_p}^2 V_{o1} V_{o2} Y_2 + {G_p}^2 I_{o1} I_{o2} Z_{g2} \\
&+ G_p I_{o2} Y_1 Z_{g2} + {G_p}^2 I_{o2} V_{o1} Y_1 Z_{g2} + G_p I_{o1} Y_2 Z_{g2} \\
&+ {G_p}^2 I_{o1} V_{o2} Y_2 Z_{g2} + Y_1 Y_2 Z_{g2} + G_p V_{o1} Y_1 Y_2 Z_{g2} \\
&+ G_p V_{o2} Y_1 Y_2 Z_{g2} + {G_p}^2 V_{o1} V_{o2} Y_1 Y_2 Z_{g2}.
\end{aligned} \tag{30}
$$

B. Validation of Sensitivity Matrix Based on Nonlinear Model

To validate the sensitivity matrix derived in Appendix A, the small-signal disturbing method as in [30] is adopted. The variable frequency (1–1000 Hz) current disturbances (0.05 p.u.) are, respectively, imposed into the current reference of each DG in the nonlinear model built in Simulink. The parameters of the system are equivalent to the previous theoretical analysis. Then, the sensitivity matrix is obtained by the corresponding voltage components dividing the current disturbances. The voltage components can be extracted with the help of the fast Fourier transform (FFT) tool in Simulink. Fig. 42 shows the frequency response of the sensitivity matrix under the grid-connected condition and islanding condition, respectively. It can be noted that the derived and measured matrixes reach a good agreement at the low-frequency band (<500 Hz). Although the small-signal model and the simplification of the current loop lead to the small deviation between the derived and measured matrixes at the high-frequency band, the selected frequency in the proposed method pays attention to the low-frequency band and the simplification contributes to reducing the system order. This means that the derived sensitivity matrix is reasonable and convenient for analysis.

REFERENCES

[1] D. E. Olivares *et al.*, "Trends in microgrid control," *IEEE Trans. Smart Grid*, vol. 5, no. 4, pp. 1905–1919, Jul. 2014.

[2] J. M. Carrasco *et al.*, "Power-electronic systems for the grid integration of renewable energy sources: A survey," *IEEE Trans. Ind. Electron.*, vol. 53, no. 4, pp. 1002–1016, Aug. 2006.

[3] X. Guan, Z. Xu, and Q. S. Jia, "Energy-efficient buildings facilitated by microgrid," *IEEE Trans. Smart Grid*, vol. 1, no. 3, pp. 243–252, Dec. 2010.

[4] R. H. Lasseter, "Smart distribution: Coupled microgrids," *Proc. IEEE*, vol. 99, no. 6, pp. 1074–1082, Jun. 2011.

[5] D. Boroyevich, I. Cvetkovic, D. Dong, R. Burgos, F. Wang, and F. Lee, "Future electronic power distribution systems a contemplative view," in *Proc. 12th Int. Conf. Optim. Elect. Electron. Equip.*, 2010, pp. 1369–1380.

[6] J. Rocabert, A. Luna, F. Blaabjerg, and P. Rodríguez, "Control of power converters in AC microgrids," *IEEE Trans. Power Electron.*, vol. 27, no. 11, pp. 4734–4749, Nov. 2012.

[7] J. Liu, Y. Miura, and T. Ise, "Comparison of dynamic characteristics between virtual synchronous generator and droop control in inverter-based distributed generators," *IEEE Trans. Power Electron.*, vol. 31, no. 5, pp. 3600–3611, May 2016.

[8] J. Kim, J. M. Guerrero, P. Rodriguez, R. Teodorescu, and K. Nam, "Mode adaptive droop control with virtual output impedances for an inverter-based flexible AC microgrid," *IEEE Trans. Power Electron.*, vol. 26, no. 3, pp. 689–701, Mar. 2011.

[9] D. Mlakić, H. R. Baghaee, and S. Nikolovski, "A novel ANFIS-based islanding detection for inverter-interfaced microgrids," *IEEE Trans. Smart Grid*, vol. 10, no. 4, pp. 4411–4424, Jul. 2019.

[10] H. Kakigano, M. Nomura, and T. Ise, "Loss evaluation of DC distribution for residential houses compared with AC system," in *Proc. Int. Power Electron. Conf.*, 2010, pp. 480–486.

[11] J. M. Guerrero, J. C. Vasquez, J. Matas, L. G. De Vicuña, and M. Castilla, "Hierarchical control of droop-controlled AC and DC microgrids—A general approach toward standardization," *IEEE Trans. Ind. Electron.*, vol. 58, no. 1, pp. 158–172, Jan. 2011.

[12] F. Nejabatkhah and Y. W. Li, "Overview of power management strategies of hybrid AC/DC microgrid," *IEEE Trans. Power Electron.*, vol. 30, no. 12, pp. 7072–7089, Dec. 2015.

[13] K. Strunz, E. Abbasi, and D. N. Huu, "DC microgrid for wind and solar power integration," *IEEE J. Emerg. Sel. Top. Power Electron.*, vol. 2, no. 1, pp. 115–126, Mar. 2014.

[14] T. Dragičević, X. Lu, J. C. Vasquez, and J. M. Guerrero, "DC microgrids—Part I: A review of control strategies and stabilization techniques," *IEEE Trans. Power Electron.*, vol. 31, no. 7, pp. 4876–4891, Jul. 2016.

[15] S. D. A. Fletcher, P. J. Norman, K. Fong, S. J. Galloway, and G. M. Burt, "High-speed differential protection for smart DC distribution systems," *IEEE Trans. Smart Grid*, vol. 5, no. 5, pp. 2610–2617, Sep. 2014.

[16] J. Do Park, J. Candelaria, L. Ma, and K. Dunn, "DC ring-bus microgrid fault protection and identification of fault location," *IEEE Trans. Power Del.*, vol. 28, no. 4, pp. 2574–2584, Oct. 2013.

[17] H. R. Baghaee, D. Mlakić, S. Nikolovski, and T. Dragicčvić, "Anti-islanding protection of PV-based microgrids consisting of PHEVs using SVMs," *IEEE Trans. Smart Grid*, vol. 11, no. 1, pp. 483–500, Jan. 2020.

[18] H. R. Baghaee, D. Mlakić, S. Nikolovski, and T. Dragicević, "Support vector machine-based islanding and grid fault detection in active distribution networks," *IEEE J. Emerg. Sel. Top. Power Electron.*, vol. 8, no. 3, pp. 2385–2403, Sep. 2020.

[19] *IEEE Standard for Interconnection and Interoperability of Distributed Energy Resources With Associated Electric Power Systems Interfaces*, IEEE Std 1547, 2018.

[20] C. Li, C. Cao, Y. Cao, Y. Kuang, L. Zeng, and B. Fang, "A review of islanding detection methods for microgrid," *Renewable Sustain. Energy Rev.*, vol. 35, pp. 211–220, Apr. 2014.

[21] D. Mlakić, H. R. Baghaee, and S. Nikolovski, "Gibbs phenomenon-based hybrid islanding detection strategy for VSC-based microgrids using frequency shift, $\mathrm{THD_U}$, and $\mathrm{RMS_U}$," *IEEE Trans. Smart Grid*, vol. 10, no. 5, pp. 5479–5491, Sep. 2019.

[22] F. Paz and M. Ordonez, "An impedance-based islanding detection method for dc grids," in *Proc. 9th IEEE Int. Symp. Power Electron. Distrib. Gener. Syst.*, 2018, pp. 1–7.

[23] Q. Sun, J. M. Guerrero, T. Jing, J. C. Vasquez, and R. Yang, "An islanding detection method by using frequency positive feedback based on FLL for single-phase microgrid," *IEEE Trans. Smart Grid*, vol. 8, no. 4, pp. 1821–1830, Jul. 2017.

[24] G. S. Seo, K. C. Lee, and B. H. Cho, "A new DC anti-islanding technique of electrolytic capacitor-less photovoltaic interface in DC distribution systems," *IEEE Trans. Power Electron.*, vol. 28, no. 4, pp. 1632–1641, Apr. 2013.

[25] A. M. I. Mohamad and Y. A. R. I. Mohamed, "Assessment and performance comparison of positive feedback islanding detection methods in DC distribution systems," *IEEE Trans. Power Electron.*, vol. 32, no. 8, pp. 6577–6594, Aug. 2017.

[26] R. W. Erickson and D. Maksimovic, *Fundamentals of Power Electronics*. New York, NY, USA: Springer, 2001.

[27] Y. Gu, X. Xiang, W. Li, and X. He, "Mode-adaptive decentralized control for renewable DC microgrid with enhanced reliability and flexibility," *IEEE Trans. Power Electron.*, vol. 29, no. 9, pp. 5072–5080, Sep. 2014.

[28] L. Xu and D. Chen, "Control and operation of a DC microgrid with variable generation and energy storage," *IEEE Trans. Power Del.*, vol. 26, no. 4, pp. 2513–2522, Oct. 2011.

[29] K. Ogata, *Modern Control Engineering*, 5th ed. Englewood Cliffs, NJ, USA: Prentice-Hall, 2010.

[30] A. M. I. Mohamad and Y. A. R. I. Mohamed, "Impedance- Based analysis and stabilization of active DC distribution systems with positive feedback islanding detection schemes," *IEEE Trans. Power Electron.*, vol. 33, no. 11, pp. 9902–9922, Nov. 2018.

[31] X. Liu, A. J. Forsyth, and A. M. Cross, "Negative input-resistance compensator for a constant power load," *IEEE Trans. Ind. Electron.*, vol. 54, no. 6, pp. 3188–3196, Dec. 2007.

[32] J. Xiao, P. Wang, and L. Setyawan, "Implementation of multiple-slack-terminal DC microgrids for smooth transitions between grid-tied and islanded states," *IEEE Trans. Smart Grid*, vol. 7, no. 1, pp. 273–281, Jan. 2016.

Qinghui Huang (Student Member, IEEE) received the B.Sc. degree from the College of Electrical and Information Engineering, Hunan University, Changsha, China, in 2014. He is currently working toward the M.Sc. degree with the College of Electrical Engineering, Zhejiang University, Hangzhou, China.

His research interests include the control and protection of dc microgrids.

Hongyi Chen (Student Member, IEEE) received the B.S. degree in electrical engineering from North China Electric Power University, Beijing, China, in 2019. She is currently working toward the M.S. degree in electrical engineering with Zhejiang University, Hangzhou, China.

Her main research interests include the control strategy of dc microgrids.

Xin Xiang (Member, IEEE) received the B.Sc. degree from the Harbin Institute of Technology, Harbin, China, in 2011, the M.Sc. degree from Zhejiang University, Hangzhou, China, in 2014, and the Ph.D. degree from Imperial College London, London, U.K., in 2018, all in electrical and electronic engineering.

From 2018 to 2020, he was a Research Associate with Imperial College London. He is currently a tenure-track Associate Professor with the College of Electrical Engineering, Zhejiang University. His research interests include the analysis and control of power electronics converters for power system applications.

Dr. Xiang was the recipient of the Eryl Cadwaladr Davies Prize for the Best Ph.D. Thesis of the Electrical and Electronic Engineering Department, Imperial College London, and the Best Ph.D. Thesis Award from the IEEE Power Electronics Society U.K. and Ireland Chapter.

Chushan Li (Member, IEEE) received the B.E.E. degree and the Ph.D. degree in electrical engineering from the Department of Electrical Engineering, Zhejiang University, Hangzhou, China, in 2008 and 2014, respectively.

He is currently an Assistant Professor with Zhejiang University–University of Illinois at Urbana-Champaign Institute, Zhejiang University, Zhejiang, China. From April to September in 2008, he was an Internship Student with the Power Application Design Center, National Semiconductor (Hong Kong) Company, Ltd., Hong Kong. From December 2010 to October 2011, he was a Visiting Scholar with the FREEDM Center, North Carolina State University, Raleigh, NC, USA. From December 2013 to June 2014, he was a Research Assistant with Hong Kong Polytechnic University, Hong Kong. From July 2014 to July 2017, he was a Postdoctoral Fellow with the Department of Electrical and Computer Engineering, Ryerson University, Toronto, ON, Canada. His research interests include high power density power converter design and transportation electrification.

Wuhua Li (Member, IEEE) received the B.Sc. and Ph.D. degrees in power electronics and electrical engineering from Zhejiang University, Hangzhou, China, in 2002 and 2008, respectively.

From 2004 to 2005, he was a Research Intern, and from 2007 to 2008, a Research Assistant with GE Global Research Center, Shanghai, China. From 2008 to 2010, he was a Postdoctoral Researcher with the College of Electrical Engineering, Zhejiang University, where, he was promoted as an Associate Professor in 2010 and has been a Full Professor since 2013. From 2010 to 2011, he was a Ryerson University Postdoctoral Fellow with the Department of Electrical and Computer Engineering, Ryerson University, Toronto, ON, Canada. He is currently the Executive Deputy Director of the National Specialty Laboratory for Power Electronics and the Vice Director of the Power Electronics Research Institute, Zhejiang University. He has authored or coauthored more than 300 peer-reviewed technical papers and holds over 50 issued/pending patents. His research interests include power devices, converter topologies, and advanced controls for high power energy conversion systems.

Dr. Li was the recipient of the 2012 Delta Young Scholar from Delta Environmental and Educational Foundation, the 2012 Outstanding Young Scholar from National Science Foundation of China (NSFC), the 2013 Chief Youth Scientist of National 973 Program, the 2014 Young Top-Notch Scholar of National Ten Thousand Talent Program, and the 2019 Distinguished Young Scholar from National Science Foundation of China, due to his excellent teaching and research contributions, as well as a National Natural Science Award and four Scientific and Technological Achievement Awards from Zhejiang Provincial Government and the State Educational Ministry of China. He is the Associated Editor for the IEEE JOURNAL OF EMERGING AND SELECTED TOPICS IN POWER ELECTRONICS, *IET Power Electronics*, *CSEE Journal of Power and Energy Systems*, *CPSS Transactions on Power Electronics and Applications*, *Proceedings of the Chinese Society for Electrical Engineering*, and a Guest Editor for the Special Issue on DC and HVDC System Technologies of *IET Renewable Power Generation*, and a Member of Editorial Board for the *Journal of Modern Power System and Clean Energy*. He was appointed as the Most-Cited Chinese Researcher by Elsevier since 2014.

Xiangning He (Fellow, IEEE) received the B.Sc. and M.Sc. degrees from the Nanjing University of Aeronautics and Astronautics, Nanjing, China, in 1982 and 1985, respectively, and the Ph.D. degree from Zhejiang University, Hangzhou, China, in 1989.

From 1985 to 1986, he was an Assistant Engineer with the 608 Institute of Aeronautical Industrial General Company, Zhuzhou, China. From 1989 to 1991, he was a Lecturer with Zhejiang University. In 1991, he obtained a Fellowship from the Royal Society of U.K., and conducted research with the Department of Computing and Electrical Engineering, Heriot-Watt University, Edinburgh, U.K., as a Postdoctoral Research Fellow for two years. In 1994, he joined as an Associate Professor with Zhejiang University, where, he has been a Full Professor with the College of Electrical Engineering, since 1996. He was the Director of the Power Electronics Research Institute, the Head of the Department of Applied Electronics, the Vice Dean of the College of Electrical Engineering, and is currently the Director of the National Specialty Laboratory for Power Electronics, Zhejiang University. His research interests include power electronics and their industrial applications.

Dr. He is a fellow of The Institute of Electrical and Electronics Engineers (IEEE) and was appointed as IEEE Distinguished Lecturer by the IEEE Power Electronics Society 2011–2015. He is also a fellow of the Institution of Engineering and Technology (formerly IEE), U.K.